# Self-generated gradients steer collective migration on viscoelastic collagen networks

Andrew G. Clark[1,10,11,✉], Ananyo Maitra[2,3,✉], Cécile Jacques[1], Martin Bergert[4],

Carlos Pérez-González[1], Anthony Simon[1], Luc Lederer[1], Alba Diz-Muñoz[4], Xavier Trepat[5,6,7,8],

Raphaël Voituriez[3,9,12] and Danijela Matic Vignjevic[1,12]

[1] *Cell Biology and Cancer Unit, Institut Curie, PSL Research University, Paris, France.*

[2] *Laboratoire Jean Perrin, Sorbonne Université and CNRS, Paris, France.*

[3] *Laboratoire de Physique Théorique et Modélisation, CNRS, CY Cergy Paris Université, Cergy-Pontoise Cedex, France*

[4] *Cell Biology and Biophysics Unit, European Molecular Biology Laboratory, Heidelberg, Germany*

[5] *Institute for Bioengineering of Catalonia, The Barcelona Institute for Science and Technology (BIST), Barcelona, Spain.*

[6] *Facultat de Medicina, University of Barcelona, Barcelona, Spain.*

[7] *Institució Catalana de Recerca i Estudis Avançats (ICREA), Barcelona, Spain.*

[8] *Centro de Investigación Biomédica en Red en Bioingeniería, Biomateriales y Nanomedicina, Barcelona, Spain.*

[9] *Laboratoire de Physique Théorique de la Matière Condensée, Sorbonne Université and CNRS, Paris, France.*

[10] *Present Address: Institute of Cell Biology and Immunology, Stuttgart Research Center Systems Biology, University of Stuttgart, Stuttgart, Germany*

[11] *Present Address: Center for Personalized Medicine, University of Tübingen, Tübingen, Germany.*

[12] *These authors contributed equally to this work: Raphaël Voituriez, Danijela Matic Vignjevic*

✉*email: andrew.clark@srcsb.uni-stuttgart.de; nyomaitra07@gmail.com.*

1

Growing evidence suggests that the physical properties of the cellular microenvironment influence cell migration. However, it is not currently understood how active physical re-modelling by cells affects migration dynamics. Here we report that cell clusters seeded on deformable collagen-I networks display persistent collective migration despite not showing any apparent intrinsic polarity. Clusters generate transient gradients in collagen density and alignment due to viscoelastic relaxation of the collagen networks. Combining theory and experiments, we show that crosslinking collagen networks or reducing cell cluster size results in reduced network deformation, shorter viscoelastic relaxation time and smaller gradients, leading to lower migration persistence. Traction force and Brillouin microscopy reveal asymmetries in force distributions and collagen stiffness during migration, providing evidence of mechanical cross-talk between cells and their substrate during migration. This physical model provides a mechanism for self-generated directional migration on viscoelastic substrates in the absence of internal biochemical polarity cues.

Collective cell migration is an essential process during development and tissue homeostasis and has also been proposed to play a role in early stages of cancer metastasis[1]. In invasive carcinomas, which comprise ∼80% of human cancers[2], small clusters of cells can "bud" away from the primary tumor and enter the stroma, connective tissue surrounding the tumor that comprises primarily collagen-I extracellular matrix (ECM) networks[3]. Tumor buds are associated with poor prognosis and enhanced metastatic potential[4–8]. However, the mechanisms by which small cell clusters migrate on collagen networks are not currently well understood.

Collagen networks are complex materials that undergo nonlinear strain stiffening and behave in a viscoelastic manner in response to cell-generated mechanical stress[9–14]. Large cell aggregates embedded in collagen networks *in vitro* can physically pull on collagen fibers, resulting in radially aligned collagen bundles that facilitate invasion of single cells into the surrounding matrix[15–17]. Such reorganization of stromal collagen networks has been associated with cancer invasiveness, and radial arrays of thick collagen bundles have been proposed to act as "highways" for tumor cell dissemination[18,19]. Previous studies suggest that the topological properties of collagen, such as collagen fiber thickness and alignment can act as a directional cue during cell migration[20–22]. However, it is currently unclear how active reorganization of collagen networks during collective migration can influence migration dynamics.

To address this, we combined long-term live imaging, traction force microscopy and theoretical modeling to ask how the viscoelastic properties of collagen networks affect network reorganization during collective cell migration and how these local changes in network topology can feed back

on migration dynamics. Our results suggest that viscoelastic relaxation in collagen gels gives rise to local gradients in collagen organization that drive spontaneous persistent migration, even in the absence of biochemical polarity cues.

**Cell clusters migrate persistently on collagen networks**

To study collective migration on collagen networks, we generated small clusters of A431 cells, an epidermoid carcinoma cell line that has previously been shown to migrate collectively[23]. We seeded fluorescently-labeled A431 cells or clusters on collagen networks (Fig. 1a, b). Clusters in the range of 500-5000$\mu$m$^2$ contained $\sim$3-30 cells (Fig. 1c), around the range associated with carcinoma metastasis ($\sim$5 cells[4,7]). To investigate how interactions with collagen networks affected cluster migration, we seeded A431 clusters on soft (0.5kPa) poly-A-acrylamide (PAA) gels coated with either a thin ($\sim$30$\mu$m) layer of polymerized collagen-I or non-polymerized monomeric collagen-I and tracked cell migration over $\sim$16h (Fig. 1d, Supplementary Videos 1, 2). During migration on collagen networks, individual cells within the cluster did not rearrange; rather, the entire cluster appear to glide along the collagen networks as a single entity (Extended Data Fig. 1a, b).

To determine whether clusters on collagen networks migrated with higher persistence (i.e. along straighter paths), we calculated the mean squared displacement (MSD) from migration trajectories (Extended Data Fig. 1c). Investigating the scaling of MSD with respect to the lag time ($t$), we observed higher crossover times from quadratic (MSD $\propto t^2$) to linear (MSD $\propto t$) scaling for clusters migrating on PAA coated with collagen networks, suggesting more persistent migration

4

on collagen networks (Extended Data Fig. 1c, d). To more easily compare the persistence across different conditions, we fit the first 300 minutes of the MSD curves with a power-law function to extract the scaling power, henceforth referred to as the "coefficient of persistence" ($\alpha$; (Fig. 1e)). We found that clusters migrating on PAA coated with collagen networks migrated faster and more persistently than clusters migrating on PAA coated with monomeric collagen (Fig. 1f).

We next investigated how varying collagen monomer concentration or substrate stiffness affected migration. At higher concentrations of monomeric collagen, ligand coverage was similar to collagen networks, while migration speed and persistence were reduced (Extended Data Fig. 2a-d). Mean speed and persistence peaked on 2kPa gels (Extended Data Fig. 2e, f), consistent with previous observations[24,25]. However, even the highest migration persistence on 2kPa PAA gels was still significantly lower than for clusters on collagen networks polymerized on PAA or glass. We next varied collagen concentration and polymerization temperature for collagen networks (Extended Data Fig. 2g, h), which are known to affect network organization[14,21,22,26]. Although migration speed and persistence varied across different collagen network conditions, migration persistence was always higher compared to cluster migration on PAA coated with monomeric collagen (Extended Data Fig. 2f, i). These data suggest that ligand density or substrate stiffness alone cannot account for the higher migration persistence on collagen networks vs. monomeric collagen.

**Migrating cell clusters are not front-back polarized**

One potential explanation for persistent collective migration on collagen networks could be front-back biochemical polarity, a common mechanism during single cell migration. Myosin-2 typically localizes to the the cell rear in front-back polarized cells, while active Rac1 localizes to leading edge protrusions[27–29]. To test for front-back polarity during cluster migration, we used a stable A431 cell line expressing a myosin-2 light chain fused to green fluorescent protein (A431 MLC-GFP). MLC was localized to the outer "cortex" of the cluster; however, we found no asymmetry in cortical MLC accumulation with respect to migration direction, suggesting that MLC was not polarized (Extended Data Fig. 3a, Supplementary Video 3). Similarly, Rac1 was localized at the cluster cortex and down-regulated at cell-cell junctions at the cluster interior (Extended Data Fig. 3b), consistent with previous findings[23] and suggesting that cell clusters behave as large "super cells". Live imaging with the Raichu-Rac biosensor for active Rac1[30] suggested that Rac1 activity was also radially symmetric during migration (Extended Data Fig. 3c). Treatment with the Rac1 inhibitor NSC23766[31] slighlty reduced migration speed, but did not affect migration persistence, suggesting that Rac1 activity is not required for persistent migration (Extended Data Fig. 3d). In addition, we found no evidence of centrosome polarization or asymmetries in cluster shape during migration, suggesting that cell clusters are radially symmetric during migration (Extended Data Fig. 4a-c). Together, these results suggest that clusters are not front-back polarized during collective migration on collagen networks.

We next tested whether adhesions or cellular ECM modification could be polarized during mi-

gration. Staining for focal adhesion (FA) markers and imaging with live FA probes revealed that clusters on collagen networks did not assemble FAs (Extended Data Fig. 5a, b). Inhibition of integrin-$\beta$1 led to rapid retraction and eventual detachment of clusters, while inhibition of matrix metalloproteinases did not affect migration dynamics (Extended Data Fig. 5c, d, Supplementary Video 4 and Supplementary Discussion). Immunostaining for Fibronectin, Collagen-IV, Laminin and Collagen-I suggested that there was no additional ECM deposition during migration (Extended Data Fig. 6a-e and Supplementary Discussion). These data suggest that clusters do not form any local gradients of deposited or degraded ECM during migration.

**Clusters generate collagen gradients during migration**

Even without additional ECM deposition, cells and groups of cells can reorganize existing collagen networks by exerting mechanical force[15–17]. To investigate local collagen network reorganization, we imaged cell cluster migration on fluorescently-labeled collagen networks and measured local filament orientation and alignment (Extended Data Fig. 7a, b). Cell clusters generated radial arrays of aligned collagen fibers around the cluster, and filament orientation was symmetric around the outside of the cluster (Extended Data Fig. 7c). In the region directly underlying the clusters, collagen was asymmetrically patterned, with a region of high collagen density offset toward the cluster rear (Fig. 2a, b; Supplementary Video 5). Analyzing collagen profiles along the migration axis, we found that clusters generate inverse gradients of collagen density and alignment during cluster migration, with a density maximum and alignment minimum that are offset toward the

cluster rear (Fig. 2c, d; Extended Data Fig. 7d, e).

Clusters migrating on pre-aligned deformable collagen networks migrated with dynamics similar to clusters migrating on isotropic collagen networks, while clusters on pre-aligned non-deformable collagen networks migrated preferentially along the alignment axis, but with reduced speed and persistence (Extended Data Fig. 7f-i). These data suggest that network deformability and collagen gradient formation promote persistent migration regardless of imposed collagen fiber alignment.

**Collagen networks are viscoelastic**

We hypothesized that collagen gradient formation could be influenced by the viscoelastic behavior of collagen networks during migration. To investigate collagen network viscoelasticity in response to cell-generated forces, we seeded cell clusters on collagen networks and rapidly removed the clusters by treatment with Trypsin and Ammonium Hydroxide ($NH_4OH$). Following cluster removal, we measured local collagen density over time and tracked collagen network movements using particle image velocimetry (PIV; Figure 2e, f; Supplementary Video 6). Collagen density relaxed on a timescale of $\tau_r \approx$ 5-10 min. To ensure that Trypsin/$NH_4OH$ treatment resulted in an instantaneous release of mechanical stress, we performed 3D displacement microscopy using thin collagen networks polymerized on PAA gels containing fluorescent beads (Fig. 2g, Supplementary Video 7). Cell clusters initially exerted radial, inward facing in-plane stresses and downward facing out-of-plane stresses. Upon cell removal, substrate displacements immediately relaxed, suggesting that the cell-generated mechanical forces were nearly instantaneously released. The relaxation

8

time of the 3D displacements was significantly shorter than the relaxation time of collagen networks (Fig. 2f, h), suggesting that collagen networks behave in a viscoelastic manner in response to stresses generated by cell clusters during migration.

**Theoretical model of migration on a viscoelastic substrate**

To investigate how collagen gradients are formed and could help drive persistent migration, we developed a theoretical model of cluster migration on a viscoelastic substrate (Fig. 3a; see also Supplementary Note 1, Supplementary Figs. 1-6). The model describes the cell cluster as an isotropic active particle whose position along a one dimensional axis is denoted by $x_c$. This active particle deforms an apolar viscoelastic substrate, causing a structural perturbation $S(x, t)$, whose equation of motion can be schematically written as

$$\tau_r \partial_t S = -S + \ell^2 \partial_x^2 S + \tau_r f g(x - x_c). \tag{1}$$

Here, $\partial_t$ and $\partial_x$ are partial derivatives with respect to time and space, respectively, $\tau_r$ is the viscoelastic relaxation time of the substrate, $\ell$ is a deformation lengthscale over which a point perturbation spreads out, $f$ is the strength of the perturbation (proportional to the total stress exerted by the cluster on the substrate) and $g(x - x_c)$ is a normalized function that represents a spatially symmetric perturbation due to the particle's activity.

The isotropic particle actively responds to the substrate perturbation via a coupling term $\zeta$, which parameterizes the active response of the cluster to the perturbation, giving the cluster velocity, $v_c$, as

$$v_c = \dot{x}_c \propto -\zeta \partial_x S|_{x_c}, \tag{2}$$

where the overdot in $\dot{x}$ denotes a time derivative. This simple model predicts that at a critical value of $\zeta_c$, the particle's velocity will display a supercritical pitchfork bifurcation (Fig. 3b). For $\zeta < \zeta_c$, $v_c = 0$ and the cluster cannot migrate persistently. However, for $\zeta > \zeta_c$, $v_c \sim \pm(\zeta - \zeta_c)^{1/2}$, implying that the cluster migrates persistently in a random direction (forward or backward). Importantly, the critical value of activity scales with the relaxation time of the substrate as $\zeta_c \sim 1/(f\tau_r^2)$, implying that increasing the relaxation time beyond a critical value $\tau_c$ at a fixed coupling $\zeta$ leads to persistent motion of the cluster (Fig. 3c). In the presence of noise, the model predicts a Brownian-like random motion for $\zeta < \zeta_c$ or $\tau_r < \tau_c$. For $\zeta > \zeta_c$ at fixed $\tau_r$ or $\tau_r > \tau_c$ at fixed $\zeta$, the model predicts persistent motion, whose persistence time increases with $\tau_r$ (Fig. 3d). Because traction force scales with cluster size[32], the intensity $f$ of the perturbation likely depends on cluster size $L$. The coupling $\zeta$ is also likely to depend on cluster size, as clusters that are small compared to the deformation length scale $\ell$ would be too small to sense a collagen gradient. Our model therefore makes two important predictions: (1) migration persistence should decrease for substrates with lower relaxation times and (2) migration persistence should be lower for small clusters (Fig. 3e).

**Decreasing viscoelastic relaxation time reduces persistence**

To test the prediction that reducing substrate relaxation time leads to reduced migration persistence, we crosslinked collagen networks using threose or glutaraldehyde and analyzed collagen density and relaxation following rapid cell removal (Fig. 4a, Supplementary Videos 8-10). Crosslinking led to reduced initial collagen density prior to cell removal and reduced viscoelastic relaxation time following cell removal (Fig. 4b). Our theoretical model predicted that reducing $\tau_r$ would lead to a more symmetric collagen density profile. Indeed, collagen density gradients on crosslinked gels were more symmetric and had lower peak magnitudes compared with controls (Fig. 4c, d, Supplementary Videos 11-13). Clusters also migrated less persistently on crosslinked networks, while migration speed was reduced only for crosslinking with glutaraldehyde (Fig. 4e, f; Supplementary Videos 14-17). In addition, wound healing speed was significantly slower on glutaraldehyde-crosslinked collagen networks (Extended Data Fig. 8a, b), suggesting that collagen network viscoelasticity is also important for other modes of collective migration.

Treatment with the collagen-modifying enzyme Lysyl Oxidase (LOX) led to increases in collagen viscoelastic relaxation time, migration speed and migration persistence, while collagen networks with higher collagen monomer concentrations exhibited reduced initial collagen densities and relaxation times (Extended Data Fig. 8c-e). Comparing migration persistence vs. collagen relaxation time across all conditions, we found that for short relaxation times, migration persistence is low and highly dependent on relaxation time. For longer collagen relaxation times, migration persistence increases and eventually saturates, confirming the first major prediction of our model (Fig. 3d, 4g).

11

**Migration persistence depends on cluster size**

Our theoretical model predicted that migration persistence should scale with cluster size, as smaller clusters produce lower traction forces. To test this, we performed 3D displacement microscopy for differently sized clusters and single cells (Fig. 5a). Smaller clusters and single cells showed reduced substrate displacement, indicating that they indeed exert less mechanical stress on the substrate (Fig. 5b). Rapid cell removal experiments revealed that both initial collagen density and collagen relaxation time were lower for smaller clusters and single cells (Fig. 5c, d, Supplementary Video 18).

The degree of collagen reorganization by single cells is highly cell type dependent. For cancer associated fibroblasts (CAFs), which are known to be highly contractile and are specialized for collagen modification[33], collagen densities before and after cell removal were higher for single CAFs compared to A431 clusters, and viscoelastic relaxation times were shorter following CAF removal (Extended Data Fig. 9a-c). These data suggest that CAFs can more efficiently and permanently remodel collagen compared to epithelial cell clusters (see also Supplementary Discussion).

To test the prediction that single A431 cells are too small to sense collagen gradients, we performed live imaging of single cells migrating on fluorescent collagen networks. The resulting collagen density profile was constant along the length of single cells, and the intensity of the collagen gradient was lower for smaller clusters (Fig. 5e, f; Supplementary Video 19). Consistent with these data and our theoretical model, smaller clusters and single cells migrated with lower mean

instantaneous speeds and lower persistence compared to larger clusters (Fig. 5g, h; Supplementary Video 20). We observed a similar difference between migration speed and persistence for clusters vs. single cells for CaCo2 cells, an epithelial colorectal cancer cell line (Extended Data Fig. 9d-f). This suggests that the dependence of persistence on cluster size is a general phenomenon.

To investigate whether imposed collagen alignment could increase the persistence of single cell migration in A431 cells to similar levels as clusters, we compared migration dynamics of clusters and single cells on thin non-deformable aligned collagen networks. Similar to the results with clusters, single cells preferentially migrated along the collagen alignment axis, but with reduced speed and persistence compared to migration on thin isotropic collagen networks (Extended Data Fig. 9g-i). Together, these data confirm the second major prediction of our model, that small clusters and single cells migrate with lower persistence compared to larger clusters.

**Traction forces are asymmetric during collective migration**

To better understand mechanical force generation during collective migration, we performed 2D traction force microscopy (TFM) on cell clusters migrating on thin collagen networks polymerized on soft PAA gels (Fig. 6a, *upper panels*; Supplementary Video 21). Clusters generated radial inward-facing tractions around the perimeter of the cluster that peaked near the cluster contour (Fig. 6a, *lower panel*). Peak tractions were higher for clusters on PAA coated with monomeric collagen vs. PAA coated with thin collagen networks and scaled with cluster size in both conditions (Extended Data Fig. 10a, b), suggesting that non-persistent migration on monomeric collagen

13

is not simply due to insufficient force generation.

Treatment of clusters with blebbistatin led to a significant reduction in 3D substrate displacements, suggesting that cell-generated stresses are largely driven by myosin-2 activity (Extended Data Fig. 10c-e). Long-term treatment with blebbistatin led to a dissolution of clusters (Extended Data Fig. 10f), consistent with previous studies[23,34]. As myosin activity drives retrograde actin flow in cellular protrusions[35], we analyzed actin flows along the migration direction in A431 cells stably expressing the fluorescent F-actin probe LifeAct-mCherry (Extended Data Fig. 10g, Supplementary Video 22). Clusters exhibited inward-facing actin flows with a slight overall bias toward rearward-facing flows (Extended Data Fig. 10h, i).

To investigate the distribution of traction forces during collective migration, we measured the peak traction magnitude with respect to the migration direction (Fig. 6b). The traction peak at the rear of the cluster was ~10% higher compared to the leading edge of the cluster (Fig. 6b, c). Traction peak asymmetry was lower for smaller clusters and single cells (Extended Data Fig. 10j), consistent with our observation that migration persistence also depends on cluster size. Projecting the tractions along the migration axis, we found that projected tractions were negative (rearward-facing) at the front and positive (forward-facing) at the rear (Extended Data Fig. 10k, l). The traction peak was slightly higher in the rear, while the tail of traction decay at the front was slightly wider, indicating an asymmetry in the distribution of traction forces at the front vs. rear of the cluster (Extended Data Fig. 10m, n). As expected from force balance, the vectorial sum of the tractions was zero. Together, these data suggest that cell clusters exhibit asymmetric traction force profiles on collagen

networks during migration.

**Clusters generate stiffness gradients during migration**

Previous studies have shown that networks with higher collagen concentrations are stiffer[12,14,36]. To determine whether local collagen density gradients generated during migration correlated with changes in collagen network mechanics, we performed Brillouin Microscopy, a purely optical technique that allows for the acquisition of 3D maps of viscoelastic properties[37,38]. We analyzed the maximum collagen density and Brillouin shift in the collagen network for different angles around the cluster (Fig. 6d, e). Regions of high collagen density correlated with regions of higher Brillouin shift (Fig. 6e, f), suggesting that cell clusters generate local gradients not only in collagen density and alignment, but also substrate stiffness, and that clusters migrate persistently down these stiffness gradients during migration.

We next asked whether the observed gradients in collagen density, stiffness and nematic order could influence protrusive activity during migration. To this end, we quantified cellular protrusions in migrating cell clusters with respect to the migration direction (Fig. 6g). Clusters typically displayed multiple simultaneous protrusions, and the average number of protrusions increased with increasing cluster area (Fig. 6h). When we compared the protrusion angles with the migration angle, we found a slight, but significant bias in protrusion localization toward the front of migrating clusters (Fig. 6i). These data suggest that the local reorganization of the collagen network during migration could bias protrusion location toward the leading edge of the cluster and thereby promote

15

persistent migration.

**Outlook**

Here we provide a simple physical mechanism for persistent collective cell migration on ECM networks that does not depend on internal biochemical polarity and can be applied to other systems, both living and artificial (see Supplementary Discussion, Supplementary Note 1). This mechanism is similar in spirit to a model showing that apolar colloidal particles can become spontaneously self-propelled and swim persistently due to hydrodynamic flows generated during particle motion[39]. The mechanism also shares similarities with a recent model of spontaneous persistent migration for cells migrating in uniform concentrations of chemokine by self-generated chemotaxis, where chemokine depletion leads to the generation of transient local gradients[40].

Several reports have shown that cells can undergo collective durotaxis, even generating stiffness gradients during migration[41–43]. Our data imply that cell clusters migrate away from regions of high collagen stiffness, suggesting that they could be undergoing "negative" durotaxis. Migration toward softer substrates has recently been described for single cells *in vitro* and *in vivo*, namely during axonal migration[44,45]. Future studies will be required to better understand the mechanistic differences between positive and negative durotaxis. One aspect of mechanosensing during migration that has been little studied is the role of substrate viscoelaticity, which is crucial for driving persistent collective migration in our study. Other recent reports have shown that substrate viscoelasticity can impact cell spreading, migration and collective behavior in both 2D and 3D en-

vironments[46–48], arguing that substrate viscoelasticity should also be considered alongside elastic stiffness.

Collective cell migration has emerged as a potential mechanism for tumor dissemination in early stages of metastasis. Although previous studies suggest that migrating as a group may offer advantages in cell survival or chemotaxis prowess[6,49,50], it has yet been unclear whether collective migration offers any specific advantage over single cell migration in stroma-like environments. The results presented here provide a mechanism for increased migration efficiency for groups of cells migrating collectively that does not require any intrinsic cell or cluster polarity, but relies simply on physical interactions with viscoelastic collagen networks. Future studies will help to uncover how this mechanism can be applied to better understand collective stromal migration during early metastasis.

**Author Contributions**   A.G.C., A.M., R.V. and D.M.V. designed the research and wrote the manuscript; A.G.C. carried out most of the experiments and image analysis; A.M. and R.V. created the theoretical model;

18

C.J. performed and analyzed some migration and 2D TFM experiments and performed some staining experiments; A.S. performed preliminary experiments; L.L. prepared and performed some staining, migration and micropatterning experiments; M.B. and A.D.-M. performed and helped analyze Brillouin Microscopy experiments; C.P.-G. and X.T. provided reagents, software and technical assistance for the TFM and 3D displacement experiments; C.P.-G. performed and analyzed the experiment measuring different monomeric collagen coatings; D.M.V. prepared and performed some staining, migration and micropatterning experiments; all authors discussed the results and manuscript.

**Competing Interests**    All authors declare that they have no competing financial interests.
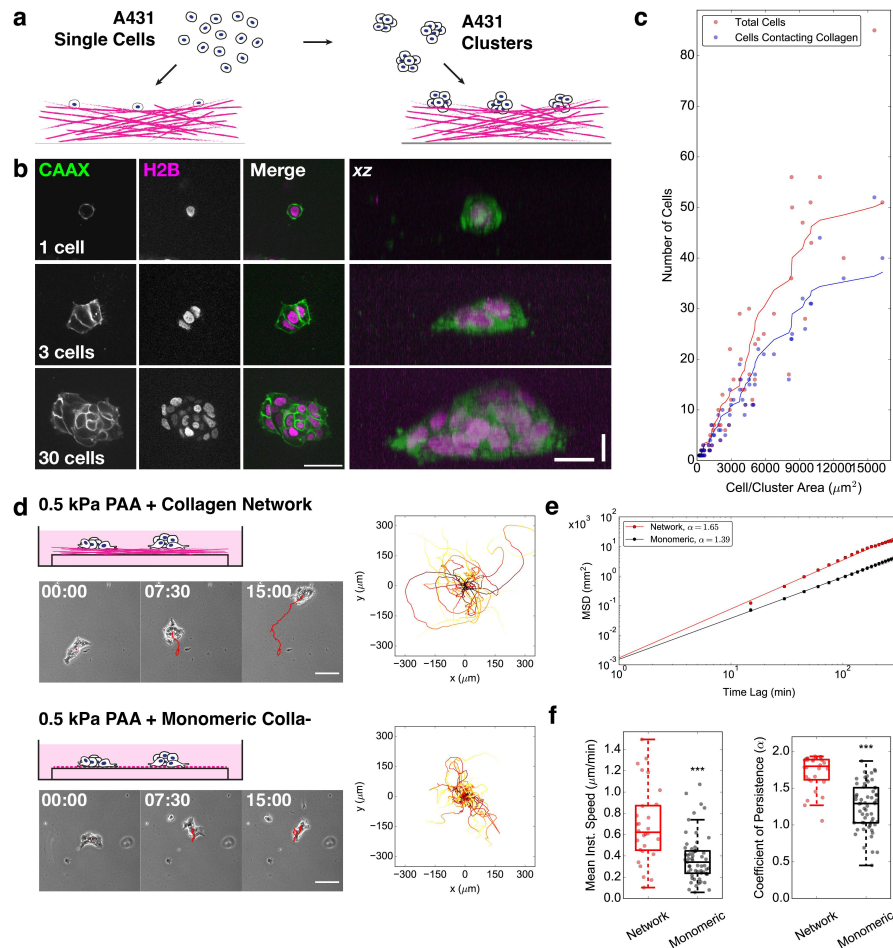
# Figures



**Fig. 1. Cell clusters migrate persistently on collagen networks. a.** Schematic showing plating of single cells or clusters on polymerized collagen-I networks. **b.** Micrographs from live imaging of stable A431 cells and different sized clusters expressing GFP-CAAX (Plasma Membrane) and mCherry-H2B (DNA). Horizontal Scale Bars: 50$\mu$m, 20$\mu$m. Vertical Scale Bar: 100$\mu$m. **c.** Plot of total number of cells and number of cells in contact with the collagen gel. Each dot represents one cluster or single cell. Solid lines: smoothed cell number vs. area data. For *b, c*, representative

20

images/data from n=71, N=2 independent experiments. **d.** *Left:* Schematics and montages of A431 cell clusters migrating on 0.5 kPa PAA gels coated with a thin 2mg/ml collagen-I network (*top panels*) or 100$\mu$g/ml monomeric collagen-I (*bottom panels*). Scale Bar: 100$\mu$m. HH:MM. See also Supplementary Videos 1, 2. *Right:* Overlaid cluster migration trajectories from clusters $\geq$500$\mu$m$^2$ and <5000$\mu$m$^2$, adjusted so that all trajectories start at the origin $(0, 0)$. **e.** Mean squared displacement (MSD) curves for cell clusters migrating on PAA gels coated with collagen network (red) or monomeric collagen (black). Data points represent mean$\pm$SEM. Solid lines represent power-law fits for the first 300min. **f.** Boxplots of mean instantaneous speed (*left*) and coefficient of persistence ($\alpha$, *right*). Coefficient of persistence was determined by fits as in *e*. Each dot represents one cluster trajectory. For *d-f*, representative images/data from n=28, 59 clusters, N=2, 3 independent experiments. ***p<0.001 for Welch's t-test (p=0.000148, 6.17e-11).
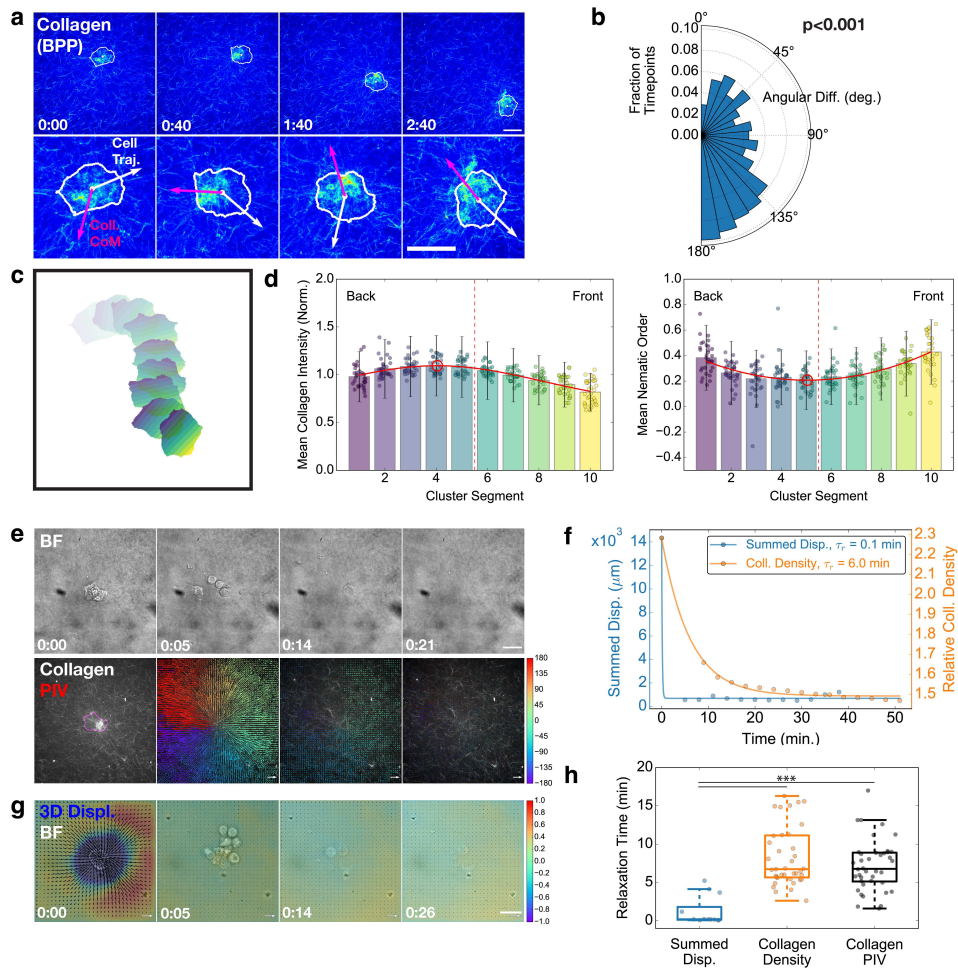
**Fig. 2. Local collagen topology is asymmetric during collective migration and relaxes viscoelastically. a.** Pseudocolor montage of fluorescent collagen (brightest point projection, BPP). White line: cluster contour. White dot: cluster center of mass. *Lower panel*: zoom from upper panel. White arrow: migration trajectory. Magenta arrow: direction of collagen center of mass. Scale Bar: 25$\mu$m. HH:MM. See also Supplementary Video 5. **b.** Polar histogram of angular difference between trajectory and collagen center of mass vectors for all timepoints. P-value: Rayleigh test of uniformity (p=2.02e-10). **c.** Segmentations from the time series in *a*, binned from the front (yellow) to the rear (violet). **d.** Bar plots of collagen intensity and alignment (nematic order) over

cluster regions (mean±SD). Red lines, Gaussian and inverted Gaussian fits to the mean values. Red circles, center position $\mu$ from fits. Each point represents one cluster averaged over time for n=34 clusters, N=5 independent experiments. **e.** Montage of brightfield and fluroescent collagen PIV vectors overlaid. Magenta: cell contour. Color Scale: displacement angle (degrees). Scale bar: 50$\mu$m. Scale vector: 0.5$\mu$m/min. HH:MM after addition of Trypsin/NH$_4$OH. See also Supplementary Video 6. **f.** Plot of summed 3D displacements (blue) and collagen density within the cell contour (orange) for experiments in *e* and *g*. Dots: individual time points. Line: exponential decay fit to extract relaxation time, $\tau_r$. **g.** Montage of 3D displacements of a cell cluster on a PAA gel coated with a thin collagen network, with cell removal after 0:00. Black arrows: in-plane (*xy*) displacements. Color scale: out-of-plane (*z*) displacements. Negative values indicate downward displacement (toward the collagen/PAA). HH:MM. Scale bar: 50$\mu$m. Scale vector: 5$\mu$m. See also Supplementary Video 7. **h.** Boxplot of $\tau_r$ from 3D substrate displacements, collagen density and collagen PIV. Each dot represents one cluster from n=12, 39, 39 clusters, N=3, 6, 6 independent experiments (density/PIV measurements taken from same data). One-way ANOVA p=3.62e-5. ***p<0.001 for post-hoc Tukey HSD test (p<0.001, <0.001, 0.110).
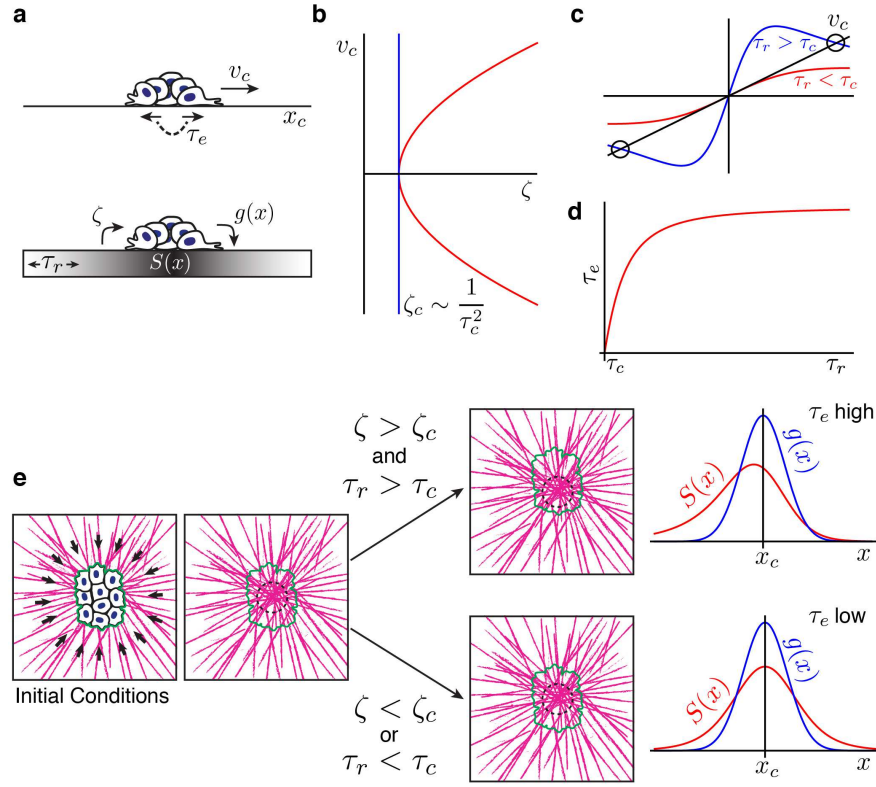
**Fig. 3. Theoretical model of persistent migration on a viscoelastic substrate. a.** Schematic description of the model. A cluster of cells moves along the axis $x_c$ with velocity $v_c$. The probability of switching migration direction is given by the timescale $\tau_e$. The cell cluster interacts with the substrate according to a symmetric forcing function $g(x)$, resulting in a deformation of the substrate given by $S(x)$. The deformation in the substrate leads to a change in the activity in the cell cluster via the coupling $\zeta$. As the substrate is viscoelastic, the relaxation is characterized by the timescale $\tau_r$. **b.** The cell migration velocity $v_c$ undergoes a supercritical pitchfork bifurcation at $\zeta = \zeta_c$. Here, $v_c$ is plotted as a function of $\zeta$ for $g(\xi') = e^{-\xi'^2/2}$. **c.** Solutions for migration velocity $v_c$ for substrate relaxation times above or below the critical relaxation time. Solutions are shown by the intersection with the black line. While for $\tau_r < \tau_c$, only a stable ($v_c = 0$) solution exists, a positive

24

solution for $v_0$ exists for $\tau_r > \tau_c$. **d.** Cluster persistence time scale $\tau_e$ as a function of the substrate relaxation time scale $\tau_r$ relative to the critical relaxation time $\tau_c$. **e.** Interpretation of the model as it relates to experiments. Initially symmetric inward-directed tractions generate radially oriented collagen fibers, with a high collagen density in the center of the cluster. After symmetry breaking, for networks with sufficient cell-substrate coupling ($\zeta > \zeta_c$) and relaxation time ($\tau_r > \tau_c$), clusters are predicted to migrate persistently (i.e. $\tau_e$ is high) due to the offset between the driving function $g(x)$ and the substrate deformation $S(x)$. If the coupling or relaxation times are below the critical values, $g(x)$ and $S(x)$ are both symmetric around $x_c$ and low persistence migration (low $\tau_e$) is predicted. Green contours: cell cluster position. Black dotted circles, collagen center of mass.

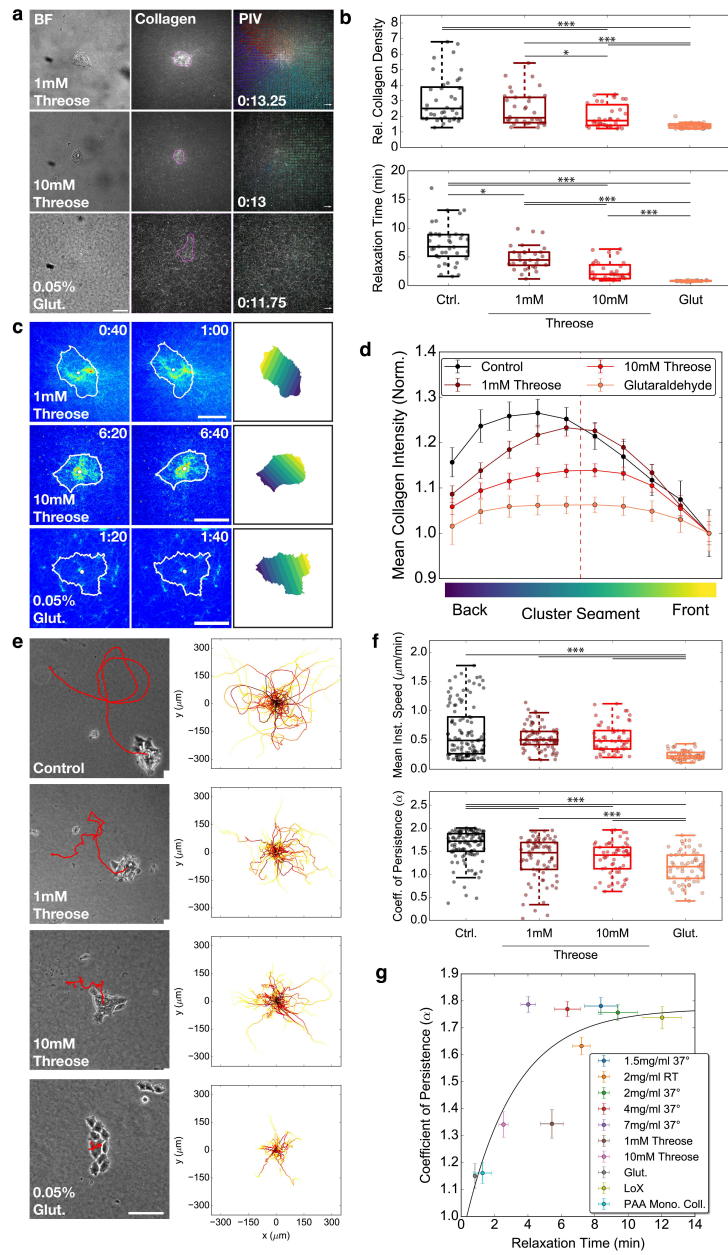**Fig. 4. Collagen crosslinking decreases viscoelastic relaxation time and reduces migration persistence. a.** Micrographs of cell clusters on fluorescent collagen networks crosslinked with threose/glutaraldehyde. Magenta: cell contour. Scale bar: 50$\mu$m. Scale vector: 0.5$\mu$m/min. HH:MM after cell removal with Trypsin/NH$_4$OH. See also Supplementary Videos 8-10. **b.** Box-

plots of collagen density and relaxation time ($\tau_r$) for conditions in *a*. Each dot represents one cluster. For *a*, *b*, representative images/data from n=39, 31, 32 clusters, N=5, 4, 4 independent experiments. One-way ANOVA p=8.21e-9, p=3.75e-14. *p<0.05, ***p<0.001 for Tukey HSD post-hoc test (p=0.559, <0.001, <0.001, 0.457, <0.001, <0.001; p=0.0412, <0.001, <0.001, <0.001, <0.001,

<0.001). **c.** Sequential timepoints of cell clusters on crosslinked fluorescent collagen networks. White line: cluster contour. White dot: cluster center of mass. Scale bar: 50$\mu$m. HH:MM. *Right*: cluster segmentation binned over the cluster length. See also Supplementary Videos 11-13. **d.** Plot of collagen intensity along the cluster length for clusters migrating on crosslinked collagen networks. For *c*, *d*, representative images/data from n=34, 30, 17 clusters, N=5, 2, 3 independent experiments (mean±SEM). Control data is the same as Fig. 2d. **e.** Brightfield micrographs from cell cluster migration on crosslinked collagen networks after 16h of migration. Red: cell trajectory. Scale bar: 100$\mu$m. *Right*: Overlaid migration trajectories for all tracked clusters, adjusted to start at the origin (0, 0). See also Supplementary Video 14-17. **f.** Boxplots of mean instantaneous speed and coefficient of persistence. Each dot represents one cluster trajectory. For *e*, *f*, representative images/data from n=91, 76, 57 clusters, N=5, 2, 2 independent experiments. One-way ANOVAs p=8.67e-12, 1.656e-13. ***p<0.001 for Tukey HSD post-hoc test (p=0.073, 0.101, <0.001, 0.881, <0.001, <0.001; p<0.001, <0.001, <0.001, 0.900, 0.00937, 0.00437). **g.** Plot of average coefficient of persistence vs. viscoelastic relaxation time for different conditions of collagen polymerization or crosslinking or PAA gels coated with monomeric collagen (PAA Mono. Coll.). Mean±SEM for each condition from n=30, 40, 30, 20, 30, 34, 34, 29, 30, 12 clusters, N=3,

5, 3, 2, 3, 4, 4, 3, 3, 2 independent experiments.
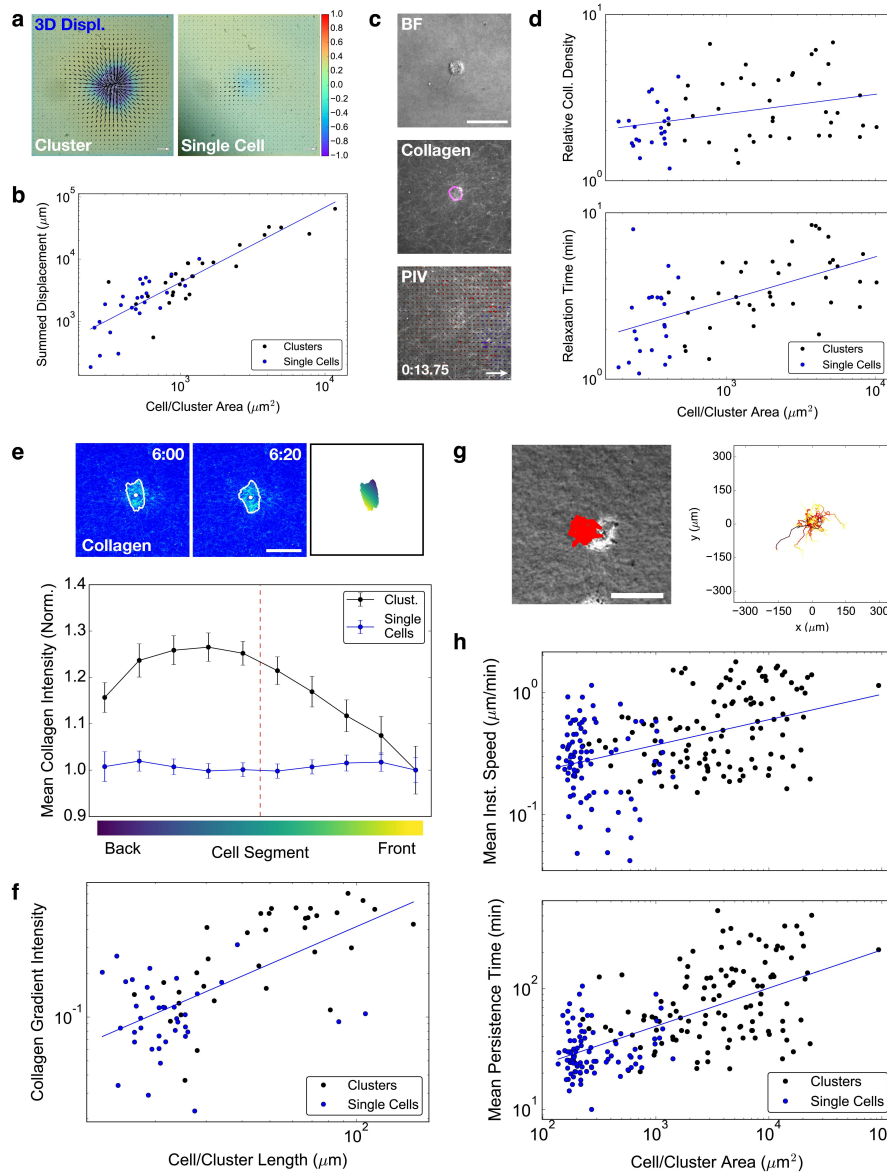
**Fig. 5. Collagen deformation and migration persistence depend on cluster size. a.** 3D displacement microscopy comparing clusters and single cells. Black arrows: *xy* displacements ($\mu$m). Color scale: *z* displacements. Scale Vector: $5\mu$m. **b.** Plot of 3D displacements vs. cluster/cell area. Blue line: power-law fit (all data). For *a, b*, representative images/data from n=27, 25 clusters/cells, N=4, 4 independent experiments. **c.** Micrograph of single cell on fluorescent collagen

network. Magenta line: cell contour. Scale bar: $50\mu$m. Scale vector: $0.5\mu$m/min. HH:MM after cell removal with Trypsin/$NH_4OH$. Representative example from n=22 cells, N=6 independent experiments. See also Supplementary Video 18. **d.** Plot of relative collagen density and relaxation time. Each dot represents one cluster or single cell. Blue line: power-law fit (all data). Data from n=38, 22 clusters/single cells, N=6, 6 independent experiments. Cluster data same as control data in Fig. 4b. **e.** Sequential timepoints of a single cell on a fluorescent collagen network. White line: cell contour. White dot: center of mass. Scale bar: $50\mu$m. HH:MM. *Right*: cell segmentation binned over cluster length. *Lower panel*: Plot of collagen intensity along cell/cluster length. Mean±SEM over all timepoints for n=34, 38 clusters, N=5, 5 independent experiments. Cluster data the same as Fig. 2d. See also Supplementary Video 19. **f.** Plot of collagen gradient intensity for single cells and clusters. For *e, f*, representative images/data from n=34, 38 clusters/single cells, N=5, 5 independent experiments. **g.** Brightfield micrograph from single cell migration on collagen network after 16h. Red: cell trajectory. *Right*: Overlaid migration trajectories adjusted to start at the origin (0, 0). Representative example from n=91 cells, N=3 independent experiments. Scale bar: $50\mu$m. See also Supplementary Video 20. **h.** Scatter plots of mean instantaneous speed and coefficient of persistence. Each dot represents one trajectory from n=91, 91 clusters/single cells, N=5, 3 independent experiments. Cluster data the same as control data in Fig. 4f.
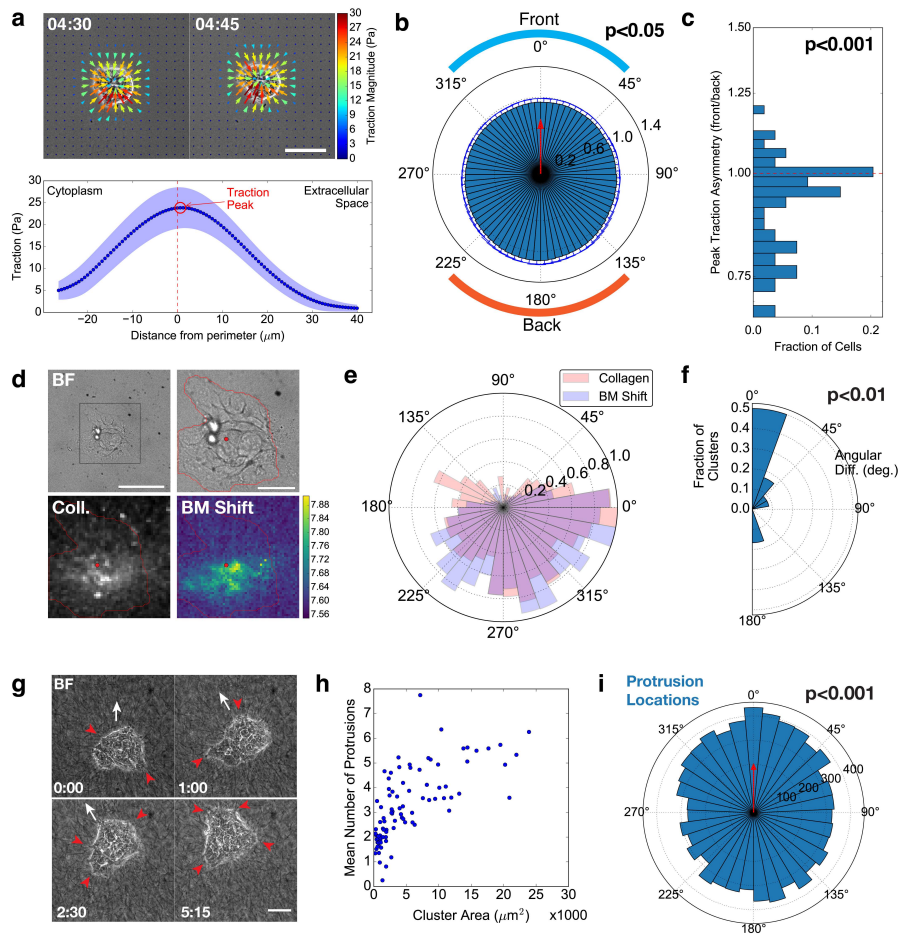
**Fig. 6. Persistent migration is associated with asymmetries in traction force distribution and collagen stiffness gradients. a.** Example micrograph overlaid with traction force vectors (arrows) for a cluster on a PAA gel + thin collagen network. Scale bar: 100$\mu$m. HH:MM. *Lower panel:* Average linescan (mean$\pm$SD) of traction forces around the cell cluster. Red dotted line: cluster periphery. Red circle: peak traction force magnitude. See also Supplementary Video 21. **b.** Polar plot of peak traction force magnitude (mean$\pm$SD) with respect to migration direction (red arrow). **c.** Histogram of peak traction force asymmetry (front quadrant / rear quadrant). Y-axis shown in log-scale. For *a-c*, representative images/data from n=27 clusters, N=3 independent experiments.

31

P-value: two-sided t-test with hypothesized mean $\mu_0 = 1$ (p=3.66e-5). **d.** Micrographs showing collagen density and Brillouin Microscopy (BM) shift (a proxy for stiffness). Red line: cluster contour. Red dot: cluster center of mass (CoM). Scale bars: $50\mu$m, $20\mu$m. **e.** Polar histogram of maximum collagen density (red) and Brillouin shift (blue) at different angles from the CoM of the cluster in *d*. Data was rescaled to the range 0-1 to exemplify regional differences. **f.** Polar histogram of the angular difference between maximum collagen density and maximum Brillouin shift. P-value: Rayleigh test of uniformity (p=0.00389). For *d-f*, representative image/data from n=13 clusters, N=3 independent experiments. **g.** Brightfield montage of a cluster migrating on a collagen network. White arrows: migration direction. Red arrowheads: protrusion locations. Scale Bar: $50\mu$m. HH:MM. **h.** Plot of mean number of simultaneous protrusions per clusters vs. cluster area. Each dot represents one cluster. **i.** Radial histogram of protrusion location relative to the migration direction (red arrow). For *g-i*, representative images/data from n=91 clusters, N=6 independent experiments. P-value: Rayleigh test of uniformity (p=2.44e-11).

# References

1. Friedl, P. & Gilmour, D. Collective cell migration in morphogenesis, regeneration and cancer. *Nat. Rev. Mol. Cell Biol.* **10**, 445–457 (2009).

2. SEER Training Modules, *Cancer as a Disease*. U. S. National Institutes of Health, National Cancer Institute. (2017). <https://training.seer.cancer.gov/disease/>.

3. Prall, F. Tumour budding in colorectal carcinoma. *Histopathology* **50**, 151–162 (2007).

4. Wang, L. M. *et al.* Tumor budding is a strong and reproducible prognostic marker in T3N0 colorectal cancer. *Am. J. Surg. Pathol.* **33** (2009).

5. Ohike, N. *et al.* Tumor budding as a strong prognostic indicator in invasive ampullary adeno-carcinomas. *Am. J. Surg. Pathol.* **34** (2010).

6. Aceto, N. *et al.* Circulating tumor cell clusters are oligoclonal precursors of breast cancer metastasis. *Cell* **158**, 1110–1122 (2014).

7. Koelzer, V. H., Zlobec, I. & Lugli, A. Tumor budding in colorectal cancer—ready for diagnostic practice? *Hum. Pathol.* **47**, 4–19 (2016).

8. Cho, S.-J. & Kakar, S. Tumor budding in colorectal carcinoma: Translating a morphologic score into clinically meaningful results. *Arch. Pathol. Lab. Med.* **142**, 952–957 (2018).

9. Pryse, K. M., Nekouzadeh, A., Genin, G. M., Elson, E. L. & Zahalak, G. I. Incremental mechanics of collagen gels: New experiments and a new viscoelastic model. *Ann. Biomed. Eng.* **31**, 1287–1296 (2003).

10. Krishnan, L., Weiss, J. A., Wessman, M. D. & Hoying, J. B. Design and application of a test system for viscoelastic characterization of collagen gels. *Tissue Eng.* **10**, 241–252 (2004).

11. Xu, B., Li, H. & Zhang, Y. Understanding the viscoelastic behavior of collagen matrices through relaxation time distribution spectrum. *Biomatter* **3**, e24651 (2013).

12. Licup, A. J. *et al.* Stress controls the mechanics of collagen networks. *Proc. Natl. Acad. Sci. USA* **112**, 9573–9578 (2015).

13. Nam, S., Hu, K. H., Butte, M. J. & Chaudhuri, O. Strain-enhanced stress relaxation impacts nonlinear elasticity in collagen gels. *Proc. Natl. Acad. Sci. USA* **113**, 5492 (2016).

14. Jansen, K. A. *et al.* The role of network architecture in collagen mechanics. *Biophys. J.* **114**, 2665–2678 (2018).

15. Shi, Q. *et al.* Rapid disorganization of mechanically interacting systems of mammary acini. *Proc. Natl. Acad. Sci. USA* **111**, 658–663 (2014).

16. Kopanska, K. S., Alcheikh, Y., Staneva, R., Vignjevic, D. & Betz, T. Tensile forces originating from cancer spheroids facilitate tumor invasion. *PLOS ONE* **11**, e0156442 (2016).

17. Staneva, R. *et al.* A new biomimetic assay reveals the temporal role of matrix stiffening in cancer cell invasion. *Mol. Biol. Cell* **29**, 2979–2988 (2018).

18. Provenzano, P. P. *et al.* Collagen reorganization at the tumor-stromal interface facilitates local invasion. *BMC Med.* **4**, 38 (2006).

19. Conklin, M. W. *et al.* Aligned collagen is a prognostic signature for survival in human breast carcinoma. *Am. J. Pathol.* **178**, 1221–1232 (2011).

20. Riching, K. M. *et al.* 3D collagen alignment limits protrusions to enhance breast cancer cell persistence. *Biophys. J.* **107**, 2546–2558 (2014).

21. Fraley, S. I. *et al.* Three-dimensional matrix fiber alignment modulates cell migration and MT1-MMP utility by spatially and temporally directing protrusions. *Sci. Rep.* **5**, 14580 (2015).

22. Sapudom, J. *et al.* The phenotype of cancer cell invasion controlled by fibril diameter and pore size of 3D collagen networks. *Biomaterials* **52**, 367–375 (2015).

23. Hidalgo-Carcedo, C. *et al.* Collective cell migration requires suppression of actomyosin at cell-cell contacts mediated by DDR1 and the cell polarity regulators Par3 and Par6. *Nat. Cell. Biol.* **13**, 49–58 (2011).

24. Peyton, S. R. & Putnam, A. J. Extracellular matrix rigidity governs smooth muscle cell motility in a biphasic fashion. *J. Cell Physiol.* **204**, 198–209 (2005).

25. Ulrich, T. A., de Juan Pardo, E. M. & Kumar, S. The mechanical rigidity of the extracellular matrix regulates the structure, motility, and proliferation of glioma cells. *Cancer. Res.* **69**, 4167 (2009).

26. Wolf, K. *et al.* Physical limits of cell migration: Control by ECM space and nuclear deformation and tuning by proteolysis and traction force. *J. Cell Biol.* **201**, 1069–1084 (2013).

27. Ridley, A. J. *et al.* Cell migration: integrating signals from front to back. *Science* **302**, 1704–1709 (2003).

28. Yam, P. T. *et al.* Actin-myosin network reorganization breaks symmetry at the cell rear to spontaneously initiate polarized cell motility. *J. Cell Biol.* **178**, 1207–1221 (2007).

29. Allen, G. M. *et al.* Cell mechanics at the rear act to steer the direction of cell migration. *Cell Systems* **11**, 286–299.e4 (2020).

30. Itoh, R. E. *et al.* Activation of Rac and Cdc42 video imaged by fluorescent resonance energy transfer-based single-molecule probes in the membrane of living cells. *Molecular and cellular biology* **22**, 6582–6591 (2002).

31. Gao, Y., Dickerson, J. B., Guo, F., Zheng, J. & Zheng, Y. Rational design and characterization of a Rac GTPase-specific small molecule inhibitor. *Proc. Natl. Acad. Sci. USA* **101**, 7618 (2004).

32. Mertz, A. F. *et al.* Scaling of traction forces with the size of cohesive cell colonies. *Phys. Rev. Lett.* **108**, 198101 (2012).

33. Gaggioli, C. *et al.* Fibroblast-led collective invasion of carcinoma cells with differing roles for RhoGTPases in leading and following cells. *Nat. Cell. Biol.* **9**, 1392–1400 (2007).

34. Pérez-González, C. *et al.* Active wetting of epithelial tissues. *Nat. Phys.* **15**, 79–88 (2019).

35. Vallotton, P., Gupton, S. L., Waterman-Storer, C. M. & Danuser, G. Simultaneous mapping

of filamentous actin flow and turnover in migrating cells by quantitative fluorescent speckle microscopy. *Proc. Natl. Acad. Sci. USA* **101**, 9660 (2004).

36. Lee, B. *et al.* A three-dimensional computational model of collagen network mechanics. *PLoS ONE* **9**, e111896 EP – (2014).

37. Scarcelli, G. & Yun, S. H. Confocal brillouin microscopy for three-dimensional mechanical imaging. *Nature Photonics* **2**, 39–43 (2008).

38. Prevedel, R., Diz-Muñoz, A., Ruocco, G. & Antonacci, G. Brillouin microscopy: an emerging tool for mechanobiology. *Nat. Methods* **16**, 969–977 (2019).

39. Michelin, S., Lauga, E. & Bartolo, D. Spontaneous autophoretic motion of isotropic particles. *Phys. Fluids* **25**, 061701 (2013).

40. Tweedy, L. *et al.* Seeing around corners: Cells solve mazes and respond at a distance using attractant breakdown. *Science* **369**, eaay9792 (2020).

41. Sunyer, R. *et al.* Collective cell durotaxis emerges from long-range intercellular force transmission. *Science* **353**, 1157–1161 (2016).

42. Barriga, E. H., Franze, K., Charras, G. & Mayor, R. Tissue stiffening coordinates morphogenesis by triggering collective cell migration in vivo. *Nature* **554**, 523 EP – (2018).

43. Shellard, A. & Mayor, R. Collective durotaxis along a self-generated stiffness gradient in vivo. *Nature* (2021).

44. Thompson, A. J. *et al.* Rapid changes in tissue mechanics regulate cell behaviour in the developing embryonic brain. *eLife* **8**, e39356 (2019).

45. Isomursu, A. *et al.* Negative durotaxis: cell movement toward softer environments. Preprint at <https://www.biorxiv.org/content/10.1101/2020.10.27.357178v1> (2020).

46. Chaudhuri, O., Cooper-White, J., Janmey, P. A., Mooney, D. J. & Shenoy, V. B. Effects of extracellular matrix viscoelasticity on cellular behaviour. *Nature* **584**, 535–546 (2020).

47. Mandal, K., Gong, Z., Rylander, A., Shenoy, V. B. & Janmey, P. A. Opposite responses of normal hepatocytes and hepatocellular carcinoma cells to substrate viscoelasticity. *Biomater. Sci.* **8**, 1316–1328 (2020).

48. Elosegui-Artola, A. *et al.* Matrix viscoelasticity controls spatio-temporal tissue organization. Preprint at <https://www.biorxiv.org/content/10.1101/2022.01.19.476771v1> (2022).

49. Malet-Engra, G. *et al.* Collective cell motility promotes chemotactic prowess and resistance to chemorepulsion. *Curr. Biol.* **25**, 242–250 (2015).

50. Shellard, A., Szabó, A., Trepat, X. & Mayor, R. Supracellular contraction at the rear of neural crest cell groups drives collective chemotaxis. *Science* **362**, 339 (2018).

# Methods

All research performed for this study were carried out in accordance with local ethical regulations. Experiments involving human samples were approved by the "Committee of Protection of Patient Rights" at Institut Curie and validated by the ethics committee of the ERC STARNEL project.

**Cell culture and preparation.** A431 cells were cultured in DMEM (Gibco/Life Technologies) supplemented with 10% fetal bovine serum (FBS; Gibco). A431 wild type cells were a gift from C. Rosse and P. Chavrier (Institut Curie) and were authenticated using the Gene Print 10 System (Promega). A431 MLC-GFP and A431 Raichu-Rac cells were a gift from T. Kato and E. Sahai (Francis Crick Institute); parental A431 lines were authenticated by short tandem repeat (STR) profiling. Stable GFP-CAAX/mCherry-H2B lines were generated following transfection using Lipofectamine 3000 (Invitrogen/LifeTechnologies) according to manufacturer instructions. GFP-CAAX and mCherry-H2B plasmids were obtained as a gift by E. Paluch and selection for stable cells was performed by treatment with G418/Hygromycin B. Stable LifeAct-mCherry, Paxillin-GFP and Zyxin-mCherry lines were generated by Lentiviral infection using the pPAX2/pMD2.G packaging system in Hek293 FT cells transfected by $CaCl_2$ with help from J. Barbazan, O. Zajac and R. Bouras. The LifeAct-mCherry plasmid was a gift from G. Montagnac. The Paxillin-GFP and Zyxin-mCherry plasmids were designed in the lab of X. Trepat. CaCo2 cells, a gift from G. Montagnac (originally ATCC), were cultured in the same manner. All cells were passaged 2-3 times per week and tested for mycoplasma every 2 weeks.

Cell clusters were prepared by adding $\sim$2x10$^6$ cells to a 10cm dish that was pre-coated with 1%

Agarose in PBS and filled with DMEM + 10% FBS + 2x Antibiotic-Antimycotic (Gibco/LifeTechnologies). Cells were cultured in these non-adherent conditions overnight prior to being seeded on substrates for imaging. Before seeding, large clusters and single cells were removed: (1) the medium containing the clusters from the agarose-coated dish was pipetted into a 15mL falcon tube, (2) large clusters were allowed to sediment for 1min before all but 0.5mL of the medium was transferred to a new 15mL falcon tube, (3) cells were centrifuged briefly at $\sim$140xg and the supernatant was discarded, (4) the pellet was resuspended in 0.5mL medium; $\sim$15-60$\mu$l cluster solution was used for seeding. For single cell experiments, cells were detached, and $2$x$10^3$ cells were seeded on collagen networks. Cells were seeded in AB+ medium (DMEM + 10%FBS + 2x Anti/Anti + 0.125% Metronidazole (w/v) + 4$\mu$g/ml Ciprofloxacin) and imaged 2-3 days after seeding.

Human primary fibroblasts were isolated from untreated colorectal cancer biopsies from patients treated at Institut Curie Hospital, Paris, with written consent of the patients. The project has been approved by the "Committee of Protection of Patient Rights" at Institut Curie and validated by the ethics committee of the ERC STARNEL project.

**Preparation of isotropic and aligned collagen networks.** For experiments with cells/clusters on collagen networks, 3.5cm diameter glass bottom dishes (WPI) were pre-coated with 3-amino-propyltrimethoxysilane (diluted 1:2 with water, Sigma-Aldrich/Merck) and glutaraldehyde (0.5% in PBS; Sigma-Aldrich/Merck) and washed well with water. 200-600$\mu$l of neutralized rat tail collagen-I solution (2mg/ml; Corning) was pipetted onto each dish and incubated at 37° C with humidity for 20min before adding 2mL AB+ medium with cells/clusters. For experiments testing

different collagen concentrations or polymerization temperature, the same procedure was followed but with the concentration/temperature specified in the experiment.

To generate thick deformable aligned collagen networks, we first prepared PDMS chambers for suspending the collagen network. PDMS (Sylgard 184; Dow) components were mixed vigorously in a 1:10 ratio, degassed by centrifugation, poured into a flat aluminium boat to a thickness of ~2.5mm and cured at 80° for 2h to overnight. Thin octoganal slabs (~0.5cm side length) were then cut out using a scalpel, and a hole was punched in the middle of the slab using a 3mm diameter biopsy punch (WPI). Slabs were then pre-stressed by inserting a sharp forceps on either side of the punched hole and stretching the PDMS slab by opening the forceps. Then, 2mg/ml neutralized rat tail collagen-I solution was prepared, and $20\mu$l was pipetted into the hole. The collagen solution was incubated at room temperature for 30min to allow for polymerization. The forceps were then removed from the PDMS slab, resulting in a relaxation to its original shape and an alignment of collagen in the direction orthogonal to the stretch. The PDMS slabs were then affixed to 3.5cm glass bottom dishes using vacuum grease, AB+ medium was added and clusters were plated on the aligned collagen networks.

To generate thin non-deformable aligned collagen networks, 3.5cm glass bottom dishes pre-coated with silane and glutaraldehyde were affixed with Patafix (UHU) to the inner edge of a larger 10cm Petri dish. 2mg/ml neutralized rat tail collagen-I solution was then prepared and kept on ice. A $67\mu$l droplet of collagen solution was pipetted onto one side of each glass bottom dish (the "top") and incubated at room temperature for 8min. The 10cm dish containing the glass bottom

dishes were then tipped at a $\sim70°$ angle downward, so that the collagen droplet ran down the glass bottom dishes by gravity. The excess collagen at the bottom of each glass bottom dish was then aspirated using a micropipette. The dishes were then incubated at 37°C to further polymerize (while remaining tipped at a $\sim70°$ angle). The dishes were then returned to room temperature and placed flat on the bench top, and the process of adding a droplet of collagen, tipping the dish and incubating was repeated two additional times. After the final collagen coating, the dishes were incubated at 37°C for 15min. AB+ medium was then added, and clusters were plated on the aligned collagen networks.

**Preparation of poly-A-acrylamide substrates.** For experiments using coated PAA gels, PAA solution for 0.5kPa gels were prepared by mixing $50\mu l$ 40% acrylamide (Bio-Rad), $7.5\mu l$ 2% bis-acrylamide (Bio-Rad), $2.5\mu l$ 10% ammonium peroxodisulfate (VWR) and $0.25\mu l$ tetramethylethylene-diamine (Euromedex) in PBS (full volume $500\mu l$). Then, $16\mu l$ of solution was pipetted onto silane/gluteraldehye-coated glass bottom dishes and covered with a round 18mm diameter coverslip. Gels were incubated for 60min before washing with PBS and removing the coverslip. For TFM experiments, $10\mu l$ 2% $0.5\mu m$ diameter green fluorescent polystyrene beads (Invitrogen/ThermoFisher) were also added.

PAA gels were coated by incubating the gel with 2mg/ml sulfo-SANPAH (Sigma-Aldrich/Merck) under ultraviolet light (365nm; 10cm from source) for 10min. The gel was then washed 2x3min with 10mM HEPES and 1x3min with PBS to remove the excess sulfo-SANPAH. For coating with thin collagen networks, $100\mu l$ of neutralized 2mg/ml collagen solution was added to cover the

PAA gel and all excess collagen solution was immediately removed. Collagen was allowed to polymerize at 37° C with humidity for 20min. For coating with monomeric collagen, the desired concentration of collagen (100$\mu$g/ml for Fig. 1, different concentrations for Extended Data Fig. 2) was diluted in 0.2% Acetic Acid and pipetted to cover the PAA gel. The dish was then incubated at 37° C with humidity for 1hr and washed briefly with PBS before adding AB+ medium and clusters.

**Immunostaining.** For immunostaining of Rac1 in cell clusters, dishes containing clusters on collagen networks were washed briefly with phosphate buffered saline (PBS) and then simultaneously fixed and extracted using a solution of 4% PFA, 5% Sucrose and 0.3% Triton X-100 in PBS for 5min at room temperature. Cells were then further fixed with 4% PFA and 5% Sucrose in PBS for 40min at room temperature before washing 2x5min with PBS. Cells were stained with a primary antibody solution of 1:100 Mouse-anti-Rac1 antibody (610650, BD Biosciences) in PBS overnight. The following day, cells were washed 5x30min with PBS-T (PBS + 0.1% Tween20) and then stained with a secondary antibody solution of 1:200 Goat-anti-MouseIgG-Alexa568 (ThermoFisher) + 1:200 DAPI + 1:200 Phalloidin-Alexa633 (ThermoFisher) in PBS overnight. Samples were then washed 5x30min with PBS-T and incubated in PBS + 2xAnti/Anti until imaging. Rac1-stained clusters were imaged in 3D using an upright spinning disc confocal (Zeiss) with a 63x dipping objective (NA 1.0) and 1$\mu$m z-steps driven by Metamorph software (version 7.8.13.0).

For immunostaining of centrosomes, cell clusters were washed briefly with PBS and fixed with 4% PFA in PBS for 40min at room temperature. Samples were then washed briefly with PBS, extracted with 0.5% Triton X-100 in PBS for 5min and then washed 3x5min in PBS. Cells were stained with

a primary antibody solution of 1:500 Rabbit-anti-Pericentrin antibody (ab4448, Abcam; gift from V. Marthiens and R. Basto) in PBS overnight. The following day, cells were washed 5x30min with PBS-T and then stained with a secondary antibody solution of 1:200 Goat-anti-RabbitIgG-Alexa568 (ThermoFisher) + 1:200 DAPI + 1:200 Phalloidin-Alexa633 (ThermoFisher) in PBS overnight. Samples were then washed 5x30min with PBS-T and incubated in PBS + 2xAnti/Anti until imaging. Pericentrin-stained clusters were imaged in 3D using an inverted Eclipse Ti-E microscope (Nikon) with Spinning disk CSU-W1 (Yokogawa) integrated in Metamorph software (version 7.10.2.240) by Gataca Systems with a 40xW immersion objective (NA 1.15) and $1\mu$m z-steps. Paxillin staining was performed using the same protocol but staining with Rabbit-anti-Paxillin (1:50, SC-5574, Santa Cruz) and Goat-anti-Rabbit-Ax647 (1:200, ThermoFisher) and imaging with a Zeiss LSM880 confocal scanning microscope with a 40xO objective (NA 1.3) driven by Zeiss ZEN software (version 2.3 SP1).

For immunostaining of ECM proteins, the collagen networks were polymerized on coverslips in a 6-well plate and cell clusters were seeded on top. 2-3 days after seeding, the samples were washed briefly with PBS and fixed with 4% PFA in PBS for 20min at room temperature. Samples were then washed 3x with PBS and stained with primary antibodies in PBS at room temperature for 1hr, washed 3x with PBS and then stained with appropriate Alexa-conjugated secondary antibodies (ThermoFisher) in PBS at room temperature for 1hr. The samples were then washed 3x with PBS and inverted into 3.5cm glass-bottom dishes prior to imaging. The following primary antibodies were used: Rabbit-anti-Fibronectin (1:100; F3648, Sigma-Aldrich/Merck), Mouse-anti-Collagen-I (1:100, C2456, Sigma-Aldrich/Merck), Mouse-anti-Collagen-IV (1:100,

col-94, Sigma-Aldrich/Merck), Rabbit-anti-Laminin (1:100, L9393, Sigma-Aldrich/Merck). Samples were imaged using an inverted Eclipse Ti-E microscope (Nikon) with Spinning disk CSU-W1 (Yokogawa) integrated in Metamorph software (version 7.10.2.240) by Gataca Systems with a 60xW immersion objective (NA 1.27). For two-photon imaging (Extended Data Fig. 6e), samples were imaged using an inverted Leica SP8 microscope coupled to a femtosecond Chameleon Vision II laser (680-1350nm; Coherent, Inc.), using a Leica 63xO immersion objective (NA1.4). Fibronectin linescans were extracted by manually segmenting clusters in FIJI in the brightfield channel and taking linescans in the fibronectin channel from points along the segmentation contour to the cluster center of mass using custom software written in Python. For each cluster, the linescans were aligned, normalized to the contour to center of mass length and averaged. For colocalization analysis of TAMRA-Collagen and Collagen-I Antibody staining, the Coloc 2 plugin in FIJI was used with Costes threshold regression. The colocalization value represents the Pearson's $r$ value (no threshold).

**Drug treatments.** Clusters were treated with NSC23766 (Sigma-Aldrich/Merck) at the specified concentrations for 1hr prior to starting imaging. Cilengitide (Selleckchem) was added to a final concentration of $1\mu$M 1hr prior to starting imaging. AIIB2 (MABT409, Sigma-Aldrich/Merck) was added to a final concentration of 5-10$\mu$g/ml 30-40min prior to starting imaging. The MMP inhibitors GM6001 (final concentration: 10$\mu$m, Calbiochem) and BB94 (final concentration: 5$\mu$m, Sigma-Aldrich/Merck) were added 30-40min prior to starting imaging. For 3D displacement experiments, Para-Nitro-Blebbistatin (Sigma-Aldrich/Merck) was added at a final concentration of 30$\mu$M after taking the initial image. The second image was taken 10min after adding the bleb-

bistatin. For live imaging experiments, Para-Nitro-Blebbistatin ($30\mu$M) was added 1 hour prior to imaging.

For crosslinking of collagen networks, Threose was diluted to a final concentration of $1\mu$M or $10\mu$M in PBS and added to polymerized collagen networks. The collagen networks were incubated for 48hrs at $37^\circ$ C before washing twice with 1xPBS for 5min. The PBS was then replaced with AB+ Medium and clusters were plated. For glutaraldehyde crosslinking, 0.05% glutaraldehyde in PBS was added to polymerized collagen networks and incubated for 1hr at room temperature, which has been shown to lead to a 2x increase in stiffness[51]. To ensure soluble glutaraldehye was completely removed, gels were then washed 3x5min with PBS, then 1hr with PBS, then overnight with PBS, then quickly rinsed twice with PBS. The PBS was then replaced with AB+ Medium and clusters were plated. For LOX treatment, collagen networks were incubated with 150ng/ml recombinant human LOX (OriGene) in PBS + 2x Anti/Anti for 5 days at $37^\circ$C[52]. The collagen networks were then washed twice with PBS before adding AB+ Medium and plating clusters.

**Imaging and analysis of migration experiments.** Two to three days after seeding cells/clusters, samples were imaged using an Inverted Eclipse Ti-E microscope (Nikon) driven by Metamorph software (version 7.8.13.0) with a motorized stage and a 10x (NA 0.3) objective for $\sim$16h. Multiple cells/clusters were imaged using the Multi-Dimensional Imaging module in Metamorph. To obtain migration trajectories, cells/clusters in brightfield timelapse images were segmented and tracked using Ilastik[53]. From the tracked segmentations, the trajectories were determined from the center of mass of the segmentation at each time frame. Cluster fusion or fission events were not included

in the analysis, and only trajectories before or after these events were considered. Mean squared displacement (MSD) curves were calculated using a Fast Fourier Transform. Crossover times were fit as in previous studies[54,55]. A linear function fit to the log-transform of the MSD (equivalent to a power-law fit of the untransformed MSD) for the first 300min to extract the coefficient of persistence. For experiments using aligned collagen networks, the orientational index (OI) was calculated by taking the ratio of the sum of the migration distance along the collagen alignment axis over the total sum of the migration distance, similar to the calculation of chemotactic index[56]. Analysis and plotting of the trajectories were performed using custom software written in Python.

Quantification of the number of cells for different sized clusters and protrusion locations was performed using the CellCounter plugin (K. De Vos) in FIJI and analyzed using custom software written in Python. Nuclear tracking for clusters was performed using custom software written in Python.

**Preparation, imaging and analysis of wound healing experiments.** Collagen networks were polymerized in glass bottom dishes and treated with 1x PBS or glutaraldehyde and thoroughly washed as described above. Circular PDMS slabs of ~1.5cm diameter and ~1.5mm thickness were prepared as described above. A scalpel was then used to cut rectangular slats 6mm tall x 2mm wide. The resulting PDMS stencils were then passivated by treating with 2% Pluronic F-127 (Sigma-Aldrich/Merck) in PBS for 1 hr, then washed 3x 5min in PBS and dried using compressed air. The collagen gels were then incubated briefly in AB+ medium and dried in ambient air for 10min, and the passivated PDMS stencils were then placed on top of the collagen gels. A431

cells were then trypsinized from their culture flask, and ~200, 000 cells diluted into $50\mu l$ AB+ medium was pipetted over each rectangular slat, and the dish was incubated at 37°C with $CO_2$ and humidity for 24hr to allow cells to attach. 2mL AB+ medium was then added to each dish and the stencils were removed carefully using a forceps 1hr before beginning imaging. Samples were imaged using an Inverted Eclipse Ti-E microscope (Nikon) with a motorized stage and a 10x (NA 0.3) objective. To capture the entire region containing the cells, a grid of *xy* positions was captured for each timepoint. Cells were imaged at 30 min time intervals for ~60h.

The *xy* positions were stitched together using the Grid/Stitching plugin[57] in FIJI, rotated and cropped appropriately. To extract wound closure speed, the image stacks were filtered with a variance filter ($\sigma = 2px$), rotated around the x-axis by 90° and the average intensity projected onto 2D to create a kymograph. From the resulting kymograph, the angle of the migrating front was measured on both sides and averaged to extract the wound closure speed speed.

**Imaging and analysis of cortical intensities during migration.** A431 MLC-GFP clusters were imaged using an inverted Eclipse Ti-E microscope (Nikon) with Spinning disk CSU-W1 (Yokogawa) integrated in Metamorph software (version 7.10.2.240) by Gataca Systems with a 40xW immersion lens (NA 1.15) and $1\mu m$ z-steps for ~16h. Multiple clusters were imaged in 3D using the Multi-Dimensional Imaging module in Metamorph. To determine cortical intensities of MLC-GFP, we first registered the 3D timelapse images in the z-axis using a custom macro in FIJI. We then segmented cluster timelapse images automatically using custom software written in Python. Briefly, each image was blurred using a Gaussian filter and thresholded using Otsu's method. The

48

segmentations were further refined using binary morphology operations to remove noise and to smooth edges. The cells were then tracked frame-to-frame to extract the trajectory using the center of mass for each segmented image. Using the segmentation, we defined the cortex as the region around the cluster periphery from the outer boundary of the cluster to a contour $5\mu$m inside of the boundary. For each cortex pixel, we determined the angle of that pixel with respect to the cluster center of mass. The cortex intensity around the cluster was then determined by finding the maximum cortex intensity value within angular bins of $10°$. This cortical intensity was normalized to the average intensity in the region of the cluster inside of the cortex. For averaging the angular cortex intensities with respect to the angle of migration, we subtracted the trajectory angle from the angle value for each cortex pixel and determined the binned cortex intensities as described above.

For imaging A431 Raichu-Rac1 clusters, collagen networks were polymerized onto 18mm diameter round no. 1.5 coverslips pre-treated with silane and glutaraldehyde and coated with 2mg/ml collagen networks as described above. Coverslips were placed collagen side up into six-well plates and clusters were plated on top in AB+ medium and allowed to attach for 2-3 days. Immediately prior to imaging, the coverslips were inverted and placed onto a 3.5cm diameter glass bottom dish containing shims made from no. 1 coverglass and affixed using vacuum grease. AB+ medium was then added and samples were transported to the microscope. Raichu1-Rac clusters were imaged with a Zeiss LSM880 confocal scanning microscope using a 63xO immersion lens (NA 1.4) driven by Zeiss ZEN software (version 2.3 SP1) using appropriate laser and filter settings for imaging YFP and CFP. Images were registered, segmented and analyzed as above for MLC-GFP to extract the cortical Rac1 activity with respect to the migration direction.

A431 LifeAct-mCherry clusters were imaged using an inverted Eclipse Ti-E microscope (Nikon) with Spinning disk CSU-W1 (Yokogawa) integrated in Metamorph software (version 7.10.2.240) by Gataca Systems with a 40xW immersion lens (NA 1.15) at 10s time intervals for $\sim$30min. Images were segmented, registered and rotated as described above. Actin flows were measured by PIV using the OpenPIV (www.openpiv.net) package in Python, with a window size of 22x22 px$^2$ ($\sim$4x4 $\mu$m$^2$) and window overlap of 11x11 px$^2$ ($\sim$2x2 $\mu$m$^2$). Spurious vectors were filtered out and the gaps were filled in by local mean interpolation. PIV analysis was restricted to cortical region of clusters (within 10$\mu$m of the outer cluster boundary). To determine actin flows in different regions, the segmentation was split into 4 quadrants with respect to the migration direction (front, rear, left, right) and the vector component along the migration aixs was determined. To determine the sum vector at each time point, the vectors from the entire cortical region were summed, and the angle of the resulting vector was quantified in the radial histogram (Extended Data Fig. 10i).

Imaging of Paxillin-GFP and Zyxin-mCherry was performed in a similar manner. Samples plated on glass substrates were plated directly on 3.5cm glass bottom dishes. Samples plated on collagen networks were plated on networks polymerized on coverslips and inverted into 3.5cm glass bottom dishes for imaging. These samples were imaged with a Zeiss LSM880 confocal scanning microscope using a 63xO immersion lens (NA 1.4) driven by Zeiss ZEN software (version 2.3 SP1).

**Analysis of centrosome position in cell clusters.** Relative centrosome positions in cell clusters were determined by segmenting the cluster volume (Phalloidin channel), nuclei (DAPI channel)

and centrosomes (Pericentrin channel) in 3D. Initially a segmentation probability map was generated for each channel using Ilastik. Each channel was segmented by thresholding the probability map and performing binary morphology operations. Each nucleus was then paired with the closest centrosome (typically adjacent to the surface of the nucleus). Centrosome orientation was defined by a unit vector from the nucleus center of mass to the centrosome center of mass for each nucleus-centrosome pair.

**Imaging and analysis of fluorescent collagen networks during migration.** Monomeric collagen-I was labeled with TAMRA as previously described[58]. For fluorescently-labeled collagen networks, TAMRA collagen was mixed with unlabeled collagen at a ratio of 1:5 and neutralized; $200\mu$l of collagen solution was pipetted onto silane/glutaraldehyde-coated glass bottom dishes and polymerized as described above. Single cells or clusters were then seeded. After 2-3 days, the cells were labeled with CellTracker Green (ThermoFisher) at 1:2000 in serum-free DMEM for 30min at 37°C with 5% $CO_2$ and humidity. Following incubation, the medium was replaced with fresh AB+ medium. Samples were imaged $\sim$1hr later by 3D spinning disc microscopy using an inverted Eclipse Ti-E microscope (Nikon) with Spinning disk CSU-W1 (Yokogawa) integrated in Metamorph software (version 7.10.2.240) by Gataca Systems with a 40xW immersion lens (NA 1.15) and $1\mu$m z-steps at 20min time intervals for $\sim$16h. Multiple cells/clusters were imaged in 3D using the Multi-Dimensional Imaging module in Metamorph.

To analyze mean collagen intensity for different collagen concentrations (monomeric or network; Extended Data Fig. 2), TAMRA collagen was used. Imaging was performed as above, and care

was taken to ensure that all imaging parameters were kept constant for all conditions imaged. Mean intensity was measured using FIJI and analyzed/visualized using custom software written in Python.

Segmentation and tracking were performed on brightest point projections of CellTracker images using a custom algorithm in Python similar to those used for A431 MLC-GFP images. To determine the angular difference between clusters and the collagen center of mass, the angle from the cluster segmentation center of mass to the weighted center of mass of the collagen intensity within the segmentation region was determined. The difference between this angle and the trajectory angle was taken to be the angular difference.

To measure the local nematic order outside of the cell region (Extended Data Fig. 7a-c), collagen fiber orientations were determined for a single $z$-slice at the surface of the collagen network using CurveAlign[59] in MATLAB (version 2014b). Next, the image frame was split into a grid of square boxes, each with a side length of 120px ($33\mu$m). Within each box, we calculated the nematic order using a nematic director $\mathbf{n}$ defined by the mean filament orientation in that region. We calculated the nematic order scalar parameter considering all fibers contained within the box and not intersecting the cluster segmentation as $S(x,t) = \frac{1}{2}\langle 3\cos^2\theta_m - 1\rangle$, where $\theta_m$ is the angular difference between each fiber orientation and the nematic director $\mathbf{n}$.

To one-dimensionalize the collagen density signature, cell segmentations at each time point were divided into ten regions of equal length from the front to the rear of the cluster, according to the angle of migration at that time step. Regions were determined by making a bounding box around

52

the segmentation, rotated with the trajectory angle, and separating this bounding box into ten equal rectangles. The segmentation pixels intersecting these rectangles were used in determining the mean collagen intensity at each region. The nematic order for each region was determined for all fiber orientations in that region (obtained using CT-FIRE) using the migration trajectory angle as the nematic director $\mathbf{n}$. The nematic order was only calculated for regions containing $>3$ filament orientations. For each time point, the collagen density and nematic order were normalized to the mean of the ten regions. The collagen density peak was determined by fitting the averaged collagen density data with a Gaussian function and extracting the center position, $\mu$. The nematic order trough was determined by fitting an inverted Gaussian function. The reported peak offset for collagen density and nematic order was taken as the relative peak position multiplied by the mean segment length. Collagen gradient intensity was defined as the min-to-max range relative to mean collagen density.

Super-resolution imaging of fluorescent collagen networks was performed by polymerizing TAMRA collgaen networks on round coverslips, plating clusters and inverting into 3.5cm glass bottom dishes, as described above. These samples were imaged with a Zeiss LSM880 confocal scanning microscope equipped with the AiryScan module using a 40xO immersion objective (NA 1.3) driven by Zeiss ZEN software (version 2.3 SP1). A brightfield image was acquired initially to determine the starting position of the clusters. Then an AiryScan image of the fluorescent collagen was taken. After 30min, a second brightfield image was acquired to determine the direction of migration. Cluster segmentation was performed as described above and fiber orientations were determined using CT-FIRE for each imaging plane. The fiber orientations from each plane were

projected onto a single 2D slice, and the nematic order was calculated as described above.

**2D traction force microscopy.** For 2D traction force experiments, cell clusters were seeded on 0.5kPa PAA gels containing fluorescent beads and coated with a thin collagen-I network as described above. Clusters and beads were imaged by brightfield and epifluorescence microscopy, respectively, overnight using an Inverted Eclipse Ti-E microscope (Nikon) driven by Metamorph software (version 7.8.13.0) with a fully motorized stage and a 10x (NA 0.3) objective. Multiple cells/clusters were imaged using the Multi-Dimensional Imaging module in Metamorph. A single $z$-slice was acquired every 15min for multiple stage positions and imaged overnight for $\sim$16h. The following day, the cells were removed by briefly rinsing with PBS and incubating for 20min in 0.5x TrypLE Express (ThermoFisher) and 1N $NH_4OH$. The dish was then briefly rinsed with PBS and the collagen-I network was removed by incubating for 20min in a solution of $\sim$50$\mu$g/ml Collagenase type 3 (Worthington Biochemical) in PBS. All incubations to remove cells and the collagen network were performed directly on the microscope, being careful not to disturb the position of the imaging dish. An additional image was then taken to serve as a reference image for measuring bead displacements. Beads displacements were extracted by PIV and tractions were calculated from displacement fields by Fourier-transform, assuming finite gel thickness using custom software in Matlab[60] (version 2014b).

Clusters were segmented and tracked over time from brightfield images using Ilastik[53]. The migration trajectories were pooled with the cluster migration data described above. Traction force linescans were extracted by cubic spline interpolation of the traction field. The linescans ran from

each contour pixel to the segmentation center of mass and extended outward $40\mu$m beyond the segmentation boundary. For averaging around a single cell, linescans were aligned to the contour boundary of each linescan. The peak traction magnitudes was taken as the highest traction value in the linescan between $20\mu$m outside of the cluster boundary and $10\mu$m inside the cluster boundary. To quantify the peak traction magnitude around the cluster according to the angle, each contour pixel was assigned an angle according to the vector pointing from the center of mass of the segmentation to the contour pixel. To average over time and many clusters, the migration trajectory angle was subtracted from each contour angle (as for the MLC-GFP analysis above), and the traction peak was averaged along binned angles to achieve a mean polar plot of the peak traction magnitude with respect to migration direction. To calculate the front-to-back ratio of peak traction magnitudes, the mean peak traction from the front quadrant ($315°$-$45°$) was divided by the mean of the peak tractions from the rear quadrant ($135°$-$225°$).

For calculating the tractions along the axis of migration, each traction vector was projected along the migration axis, and the magnitude of this projected vector was plotted. Linescans of the projected tractions were generated by making a bounding box of 500px x 500px ($\sim 320\mu$m x $320\mu$m) to fit around the segmented cluster. The bounding box was then split into 500 regions from the front to the back, and the tractions (expanded to the image grid by nearest neighbor interpolation) within each segment were averaged (mean) to determine the traction value at each point along the cluster length. The raw values were smoothed using a moving window with size = 21px. To include the linescan edges in the smoothed data, the linescan was padded at the start and end using the start and end values, respectively. The linescan was then cropped to start and end when the

data reached 0.

**3D deformation microscopy.** 3D deformation microscopy experiments were set up in the same way as for 2D traction force experiments. Single cells or cell clusters were seeded on 0.5kPa PAA gels containing fluorescent beads and coated with a thin collagen-I network. Samples were imaged by 3D spinning disc microscopy using an Inverted Eclipse Ti-E microscope (Nikon) with Spinning disk CSU-W1 (Yokogawa) integrated in Metamorph software (version 7.10.2.240) by Gataca Systems with a 40xW immersion lens (NA 1.15). A single 3D stack with $1\mu$m z-steps was collected. Then the cells and collagen network were detached as described above, and a reference image stack was collected. Bead displacements along the $x$, $y$ and $z$ axes were extracted by a custom 3D PIV algorithm in Matlab. The summed displacement was the sum of the magnitude of all $xyz$ vectors in the imaging frame.

**Collagen and stress relaxation following cell removal.** To determine the collagen relaxation timescale, cells or clusters were seeded on TAMRA-collagen networks as described above. A single 3D image stack was recorded by spinning disc microscopy for each cell or cluster, with 35 $2\mu$m z-steps. Cells were then removed by treatment with 0.5x TrypLE Express and 1N $NH_4OH$. Imaging was resumed as soon as possible after the sample was stable (5-10min), noting precisely the time between cell removal and restarting imaging. Cell or cluster regions were segmented manually based on the first (pre-Trypsin/$NH_4OH$) image. The collagen density at each time point was taken as the mean intensity of a brightest point projection of the collagen intensity within the segmentation region normalized to a reference region with the same shape as the segmentation.

56

PIV analysis of collagen relaxation for sequential frames was performed using the openPIV library in Python. To determine the relaxation of stresses on the substrate following cell removal, 3D deformation microscopy was performed as described above. A single 3D image stack of clusters or single cells and their underlying collagen network/PAA gel was recorded by spinning disc microscopy as described above. Cells were then removed using Trypsin/$NH_4OH$ and imaging was resumed after 5-10min. Time 0:00 refers to frame prior to addition of Trypsin/$NH_4OH$. The relaxation timescale $\tau_r$ was extracted by fitting the displacement/density/PIV data over time with the exponential decay function $I = A \exp(-t/\tau) - C$, where A and C are constants used for fitting.

**Brillouin Microscopy** Brillouin microscopy (BM) is a purely optical technique that allows for the acquisition of 3D maps of viscoelastic properties with diffraction limited resolution[37,38]. This technique is based on Brillouin scattering, the interaction of monochromatic laser light with thermally excited, spontaneous sound waves in the GHz frequency range that exists in all matter. Due to this interaction, a small amount of the laser light exchanges energy with the sound waves and thus obtains a change in frequency. This change in frequency, termed "Brillouin shift", is given by:

$$\nu_B = \frac{2n}{\lambda_0} V \sin \frac{\theta}{2},$$

(3)

where $n$ is the refractive index within the interaction volume, $\lambda_0$ is the wavelength of the laser in vacuum, $\theta$ is the angle between incident and scattered light and $V$ is the speed of sound. Importantly, the speed of sound $V$ is related to the real part of the longitudinal modulus $M'$, a measure of stiffness, and is defined as the ratio of stress to strain in a uniaxial strain state:

$$M' = \rho V^2.$$

(4)

To determine the elastic modulus $M'$, the knowledge of the refractive index $n$ and the density $\rho$ is required. However, it was shown that in most biological samples $n$ and $\rho$ are correlated to within an error of a few percent, thus not affecting the value of $M'$ (Refs.[61,62]). Therefore, in the absence of own in-situ measures of $n$ and $\rho$, we report the Brillouin shift as the proxy for stiffness as it is the quantity measured in our experiments. Regions within an image displaying a higher Brillouin shifts are thus relatively stiffer.

Brillouin images were acquired using a custom-built confocal Brillouin microscope based on a commercial Axiovert 200 body (Zeiss) coupled with a 532nm laser and a custom-built 2-VIPA spectrometer, as described in more detail previously[63]. The intensity of the laser light was adjusted to <10mW on the sample to avoid photodamage. The light was focused using 40xW immersion objective (NA 1.2). The images were acquired by scanning the sample with an $xy$ step size of $2\mu$m and an acquisition time of 100ms per pixel. Fluorescence confocal images of the collagen were acquired immediately before Brillouin images with an $xy$ step size of $1\mu$m.

To analyze the BM shift in different regions of each cluster, we mapped rays from the cluster center of mass to the cluster periphery at every integer degree angle (360 rays) and measured the maximum BM shift for each angle. These maximum BM shifts were then binned into 10 degree regions by taking the mean. The same approach was taken for measuring the collagen density at different angles. Then, the central angle of the bins with maximal BM shift and collagen density were compared to calculate the angular difference between maximum BM shift and maximum collagen density.

**Preprocessing, image analysis, statistics and visualization.** Preprocessing of image stacks was performed using custom macros in FIJI/ImageJ[64]. For image and data analysis and visualization in Python, the Anaconda distribution of python3.7 with the following packages were used: astropy (v3.1), matplotlib (v3.0.2), numpy (v1.21.5), opencv (v3.4.2), openpiv (v0.21.2), pandas (0.23.4), pillow (v5.3.0), scikit-image (v0.17.2), scikit-learn (v0.20.1), scipy (v1.1.0), shapely (v1.6.4), tiff-file (v2020.7). For boxplots, dots represent individual measurements as described in the figure legends. Boxes represent the interquartile range (IQR; Q1 to Q3) and the line represents the median. Whiskers extend to the furthest point within 1.5*IQR away from Q1 or Q3. For exact p-values reported in legends, the order of values represents the pair-wise combinations from left to right (e.g. for 3 categories, p="1 vs. 2", "1 vs. 3", "2 vs. 3"). All Welch's t-test make no assumptions of equal variance and are two-sided.

**Data availability** The authors declare that all data supporting the findings of this study are available within the paper and its supplementary information files and from the corresponding authors upon reasonable request. A minimum data set has been uploaded to the following public repository: https://doi.org/10.5281/zenodo.6390650.

**Code availability** Custom software used to analyze images and data will be made available upon reasonable request.

# References

51. Sherlock, B. E. *et al.* Nondestructive assessment of collagen hydrogel cross-linking using time-resolved autofluorescence imaging. *J. Biomed. Opt.* **23**, 1–9 (2018).

52. Baker, A.-M., Bird, D., Lang, G., Cox, T. R. & Erler, J. T. Lysyl oxidase enzymatic function increases stiffness to drive colorectal cancer progression through fak. *Oncogene* **32**, 1863–1868 (2013).

53. Berg, S. *et al.* ilastik: interactive machine learning for (bio)image analysis. *Nat. Methods* **16**, 1226–1232 (2019).

54. Selmeczi, D., Mosler, S., Hagedorn, P. H., Larsen, N. B. & Flyvbjerg, H. Cell motility as persistent random motion: Theories from experiments. *Biophys. J.* **89**, 912–931 (2005).

55. Maiuri, P. *et al.* Actin flows mediate a universal coupling between cell speed and cell persistence. *Cell* **161**, 374–386 (2015).

56. Moghe, P. V., Nelson, R. D. & Tranquillo, R. T. Cytokine-stimulated chemotaxis of human neutrophils in a 3-D conjoined fibrin gel assay. *J. Immunol. Methods* **180**, 193–211 (1995).

57. Preibisch, S., Saalfeld, S. & Tomancak, P. Globally optimal stitching of tiled 3D microscopic image acquisitions. *Bioinformatics* **25**, 1463–1465 (2009).

58. Geraldo, S., Simon, A. & Vignjevic, D. M. Revealing the cytoskeletal organization of invasive cancer cells in 3D. *J. Vis. Exp.* e50763 (2013).

59. Bredfeldt, J. S. *et al.* Computational segmentation of collagen fibers from second-harmonic generation images of breast cancer. *J. Biomed. Opt.* **19**, 16007 (2014).

60. Trepat, X. *et al.* Physical forces during collective cell migration. *Nat. Phys.* **5**, 426–430 (2009).

61. Scarcelli, G., Pineda, R. & Yun, S. H. Brillouin optical microscopy for corneal biomechanics. *Invest. Ophthalmol. Vis. Sci.* **53**, 185–190 (2012).

62. Schlüßler, R. *et al.* Mechanical mapping of spinal cord growth and repair in living zebrafish larvae by brillouin imaging. *Biophys. J.* **115**, 911–923 (2018).

63. Bevilacqua, C., Sánchez-Iranzo, H., Richter, D., Diz-Muñoz, A. & Prevedel, R. Imaging mechanical properties of sub-micron ecm in live zebrafish using brillouin microscopy. *Biomed. Opt. Expr.* **10**, 1420–1431 (2019).

64. Schindelin, J. *et al.* Fiji: an open-source platform for biological-image analysis. *Nat. Methods* **9**, 676–82 (2012).
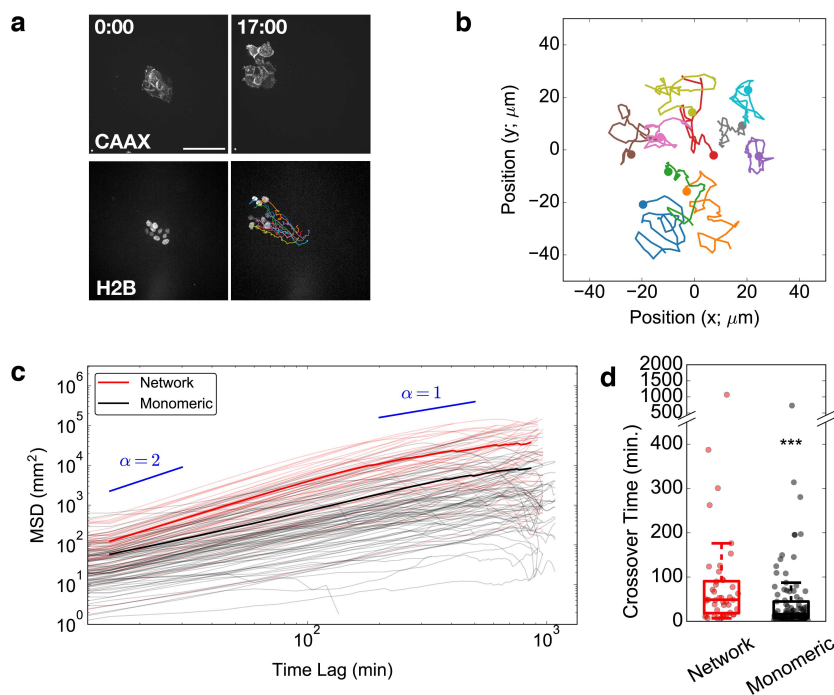
**Extended Data Fig. 1. Analysis of cell rearrangement and MSD. a.** Montage from live imaging

of stable A431 cells expressing GFP-CAAX (Plasma Membrane marker) and mCherry-H2B (DNA

marker). Colored lines are trajectories of tracked nuclei over the course of 17 hours of imaging.

Representative image from n=43 clusters imaged over N=2 independent experiments. Scale Bar:

$100\mu$m. **b.** Plot of the relative nuclear movements from *a*, registered to the migration of the whole

cluster over time. **c.** Plot of the MSD curves from all trajectories of clusters migrating on PAA

gels + collagen networks (red) or PAA gels + monomeric collagen (black). Individual trajectories

are shown in translucent colors. Solid colored lines reflect mean MSD curves. Blue lines indicate

slopes for power laws with exponents of $\alpha = 2$ or $\alpha = 1$. **d.** Crossover time from fits of individual

MSD curves. For *c*, *d*, data from n=28, 59 clusters, N=2, 3 independent experiments. ***p<0.001

for Tukey HSD test (p=0.0319).
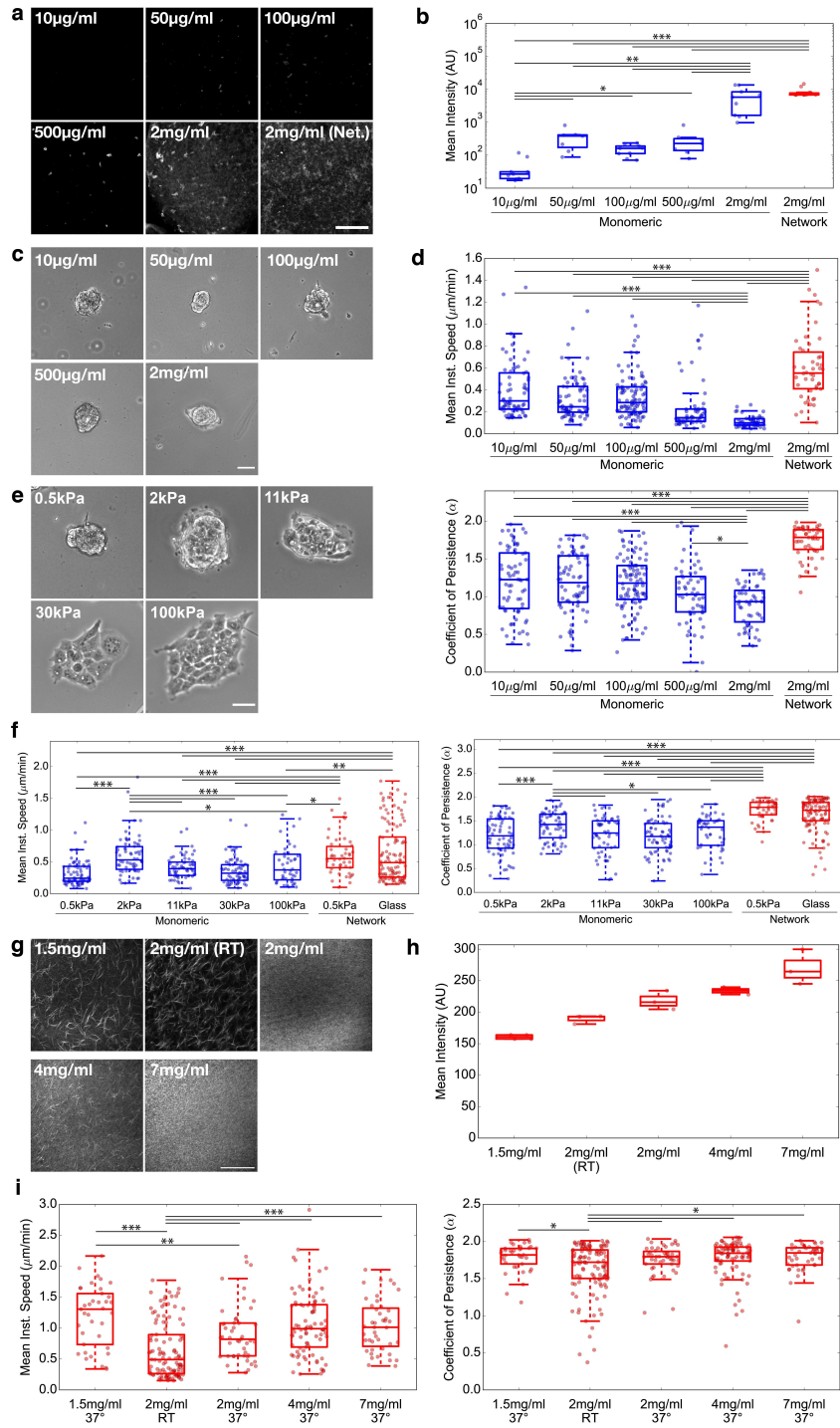
**Extended Data Fig. 2. Analysis of PAA gel stiffness and collagen concentration. a.** Repre-

sentative micrographs from PAA gel coated with different concentrations of fluorescently-labeled monomeric collagen or 2mg/ml collagen networks. Scale bar: 30$\mu$m. **b.** Boxplot of mean collagen intensity for conditions shown in *a*. Each point represents one imaging field, relative to background fluorescence in areas with no coating. For *a*, *b*, images/data from n=5 positions per condition from one representative experiment, N=3 independent experiments. One-way ANOVA p=2.10e-11. *p<0.05, **p<0.01, ***p<0.001 for Tukey HSD post-hoc test (p=0.00199, <0.001, 0.0101, 0.00162, <0.001, 0.0305, 0.679, 0.00717, <0.001, 0.121, 0.00186, <0.001, 0.00674, <0.001, 0.248).

**c.** Example micrographs of cell clusters plated on PAA gels with different concentrations of monomeric collagen. Scale bar: 50$\mu$m. **d.** Boxplots of mean instantaneous speed and coefficient of persistence for conditions in *c*. Data represents n=68, 72, 97, 56, 52, 46 clusters, N=3, 3, 3, 3, 2, 2 independent experiments. Data for collagen network and 100$\mu$g/ml monomeric collagen is the same data as presented in Fig. 1f. One-way ANOVA p=1.68e-20, 2.42e-25. *p<0.05, **p<0.01 for Tukey HSD post-hoc test (p=0.0304, 0.0368, 0.00153, <0.001, 0.00795, 0.659, 0.0547, <0.001, <0.001, 0.0145, <0.001, <0.001, <0.001, <0.001, <0.001; p=0.855, 0.773, 0.0490, <0.001, <0.001, <0.900, 0.0518, <0.001, <0.001, 0.0383, <0.001, <0.001, 0.0253, <0.001, <0.001). **e.** Example micrographs of cell clusters plated on PAA gels of different stiffness (100$\mu$g/ml monomeric collagen). Scale bar: 50$\mu$m. **f.** Boxplots of mean instantaneous speed and coefficient of persistence for conditions in *e*. Data represents n=72, 62, 57, 69, 46, 46, 114 clusters, N=3, 3, 3, 3, 3, 2, 6 independent experiments. Data for collagen network and 100$\mu$g/ml monomeric collagen is the same data as presented in Fig. 1f. One-way ANOVA p=6.26e-13, 6.25e-

30. *p<0.05, **p<0.01, ***p<0.001 for Tukey HSD post-hoc test (p<0.001, 0.00688, 0.238, 0.00704, <0.001, <0.001, <0.001, <0.001, 0.0122, 0.889, 0.564, 0.137, 0.504, <0.001, <0.001, 0.0758, <0.001, <0.001, 0.0143, 0.00996, 0.700; p=<0.001, <0.001, 0.728, 0.850, 0.233, <0.001, <0.001, 0.00300, <0.001, 0.0327, <0.001, <0.001, 0.589, 0.427, <0.001, <0.001, 0.158, <0.001, <0.001, <0.001, <0.001, 0.0763). **g.** Representative micrographs of fluor-escently-labeled collagen networks with different collagen concentration or polymerization temperature. Scale bar: $100\mu$m. **h.** Boxplot of mean collagen intensity for conditions shown in *g*. For *g*, *h*, representative images/data from n=4, 3, 3, 3, 3 positions, N=1 experiment. One-way ANOVA p=7.74e-6. **i.** Boxplots of mean instantaneous speed and coefficient of persistence for cluster migration on collagen network conditions in *g*. Data represents n=37, 114, 47, 85, 43 clusters, N=2, 3, 6, 3, 2 independent experiments. Data for 2mg/ml 37° C is the same data as presented in Fig. 1f. One-way ANOVA p=6.56e-12, 0.000609. *p<0.05, **p<0.01, ***p<0.001 for Tukey HSD post-hoc test (p<0.001, 0.00918, 0.175, 0.121, <0.001, <0.001, <0.001, 0.111, 0.206, 0.793; p=0.0134, 0.58, 0.812, 0.893, 0.0217, 0.00226, 0.00612, 0.775, 0.468, 0.705).
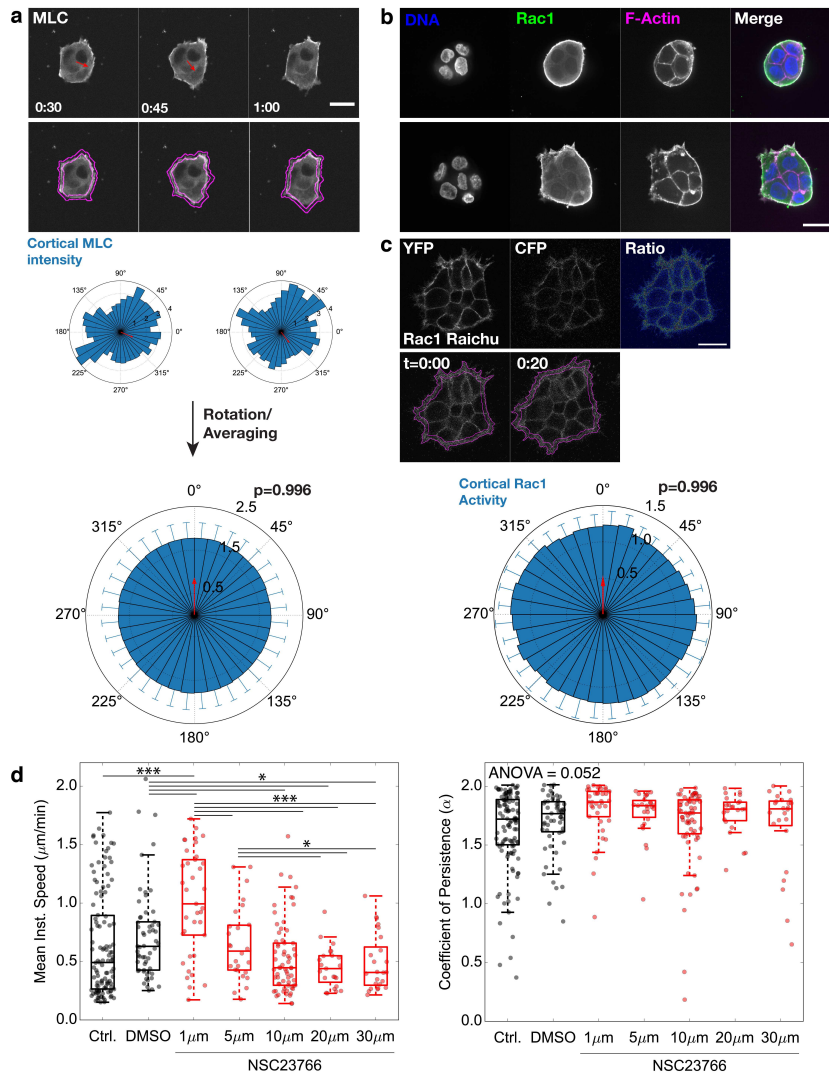
**Extended Data Fig. 3. Clusters lack front-back polarity during migration. a.** Montage from time-lapse of a myosin light chain (MLC)-GFP expressing A431 cell cluster. MLC-GFP intensity was measured in the peripheral cortical region (segmentation in magenta) around the perimeter of the cluster. See also Supplementary Video 3. At each time point, the relative cortical intensity was measured for different angles around the perimeter (blue bars) as well as the cluster trajectory (red arrow). *Lower panel*: The relative cortical intensity of myosin (mean±SD), averaged over all

time points for n=39 clusters, N=3 independent experiments. Scale bar: 25$\mu$m. p-value reflects Rayleigh test of uniformity. **b.** Fixed cell clusters plated on a collagen network and immunostained for Rac1 GTPase with DAPI (DNA) and Phalloidin (F-Actin). Shown are two representative examples from n=21 clusters and N=3 independent experiments. Scale bar: 25$\mu$m. **c.** *Upper panels*: Single time point from a live imaging experiment using Raichu-Rac1 showing YFP:CFP ratio. *Middle panels*: Micrographs of YFP:CFP ratio for two successive time points with segmentation of the cortical region (magenta lines). *Lower panel*: The cortical YFP:CFP ratio for Raichu-Rac1 (mean$\pm$SD) with respect to the migration direction (red arrow), averaged over all time points for n=8 clusters, N=3 independent experiments. Scale bar: 25$\mu$m. **d.** Boxplots of mean instantaneous speed and coefficient of persistence for cluster migration on collagen network conditions with the Rac1 inhibitor NSC23766. Data represents n=114, 57, 37, 26, 65, 23, 24 clusters, N=6, 3, 2, 1, 3, 1, 1 independent experiments. Control data is the same data as presented in Fig. 1f. For left panel, one-way ANOVA p=9.58e-9. *p$<$0.05, ***p$<$0.001 for Tukey HSD post-hoc test (p=0.243, $<$0.001, 0.893, 0.0858, 0.0508, 0.1155, 0.00143, 0.430, 0.00304, 0.00205, 0.00844, $<$0.001, $<$0.001, $<$0.001, $<$0.001, 0.0949, 0.0103, 0.0497, 0.238, 0.552, 0.549).
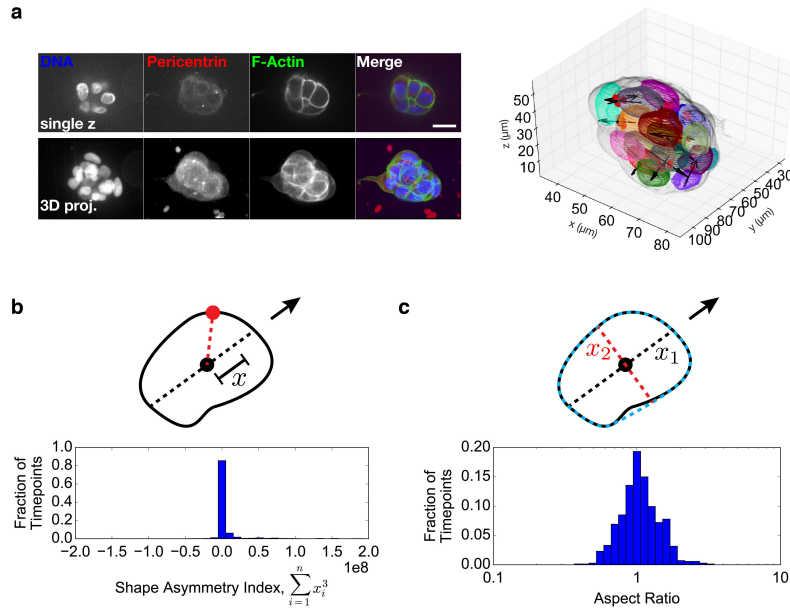
**Extended Data Fig. 4. Analysis of centrosome positioning and shape symmetry. a.** Single $z$-slice and 3D projection of a cell cluster on a collagen network with pericentrin staining. Scale bar: $20\mu$m. *Right*: Rendering of the 3D segmented nuclei (multicolor), cluster (gray) and paired centrosomes (red). Black arrows: centrosome orientation with respect to paired nucleus. Representative example from n=7 clusters, N=1 independent experiment. **b.** Shape asymmetry quantification. A center line (dotted black line) is drawn along the cluster length passing through the center of mass and parallel with the migration direction. At every pixel along the contour (red dot, e.g.), the distance $x$ from the center of mass projected onto the center line is determined. The shape asymmetry index is calculated for each time frame as the sum of $x^3$ over all contour points. *Lower panel*: histogram of the shape asymmetry from n=34 cells, N=5 independent experiments. **c.** Aspect ratio quantification. Using the Hull convex of the contour (blue dotted line) to minimize shape irregularities, the major axis $x_1$ (dotted black line) is taken as the cluster diameter along the migration

direction and passing through the center of mass (black dot). The minor axis $x_2$ (dotted red line) is taken as the cluster diameter perpendicular to the migration direction and passing through the contour center of mass. The aspect ratio is $x_1/x_2$. *Lower panel*: histogram of the aspect ratio from n=34 clusters, N=5 independent experiments.
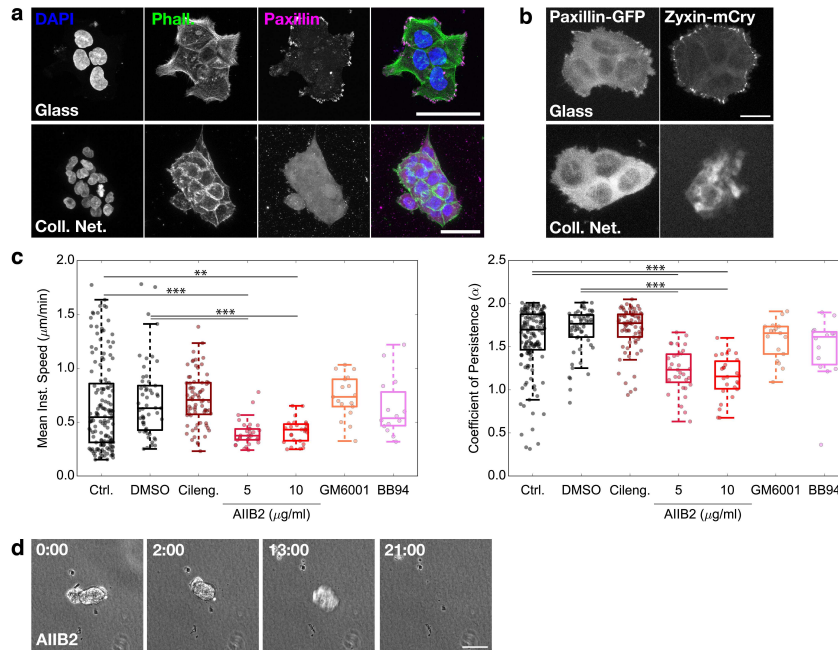
**Extended Data Fig. 5. Analysis of focal adhesions and integrins during migration. a.** Fixed cell clusters plated on glass or on a collagen network and immunostained for Paxillin with DAPI (DNA) and Phalloidin (F-Actin) counterstaining. Representative examples, N=2 independent experiments. Scale bars: $50\mu$m. **b.** Single time points from live imaging of A431 cells stably expressing Paxillin-GFP or Zyxin-mCherry, plated on glass or collagen networks. Representative examples, N=3 independent experiments. Scale bar: $50\mu$m. **c.** Boxplots of mean instantaneous speed and coefficient of persistence for cluster migration on collagen networks with the integrin binding inhibitors Cilengitide and AIIB2 and MMP inhibitors GM6001 and BB94. Data represents n=146, 57, 72, 31, 26, 17, 14 clusters, N=8, 3, 4, 2, 2, 1, 1 independent experiments. Control data is pooled from data presented in Fig. 1f. One-way ANOVAs: p=4.36e-6, 1.76e-18. **p<0.01, ***p<0.001 for Tukey HSD post-hoc test (p=0.268, 0.126, <0.001, 0.00492, 0.390, >0.9, 0.832, <0.001, <0.001, 0.865, 0.447, <0.001, <0.001, >0.9, 0.256, 0.537, <0.001, <0.001, <0.001,

<0.001, 0.243; p=0.0788, 0.0195, <0.001, <0.001, 0.88, 0.25, 0.689, <0.001, <0.001, 0.130, 0.016,

<0.001, <0.001, 0.061, 0.00522, 0.268, <0.001, 0.0148, <0.001, 0.00246, 0.354). **d.** Example micrograph from a cell cluster on a collagen network following treatment with the Integrin-$\beta$1 functional antibody AIIB2 (10$\mu$g/ml). Scale bar: 100$\mu$m. HH:MM. See also Supplementary Video 4. Representative image series from n=26 clusters, N=2 independent experiments.
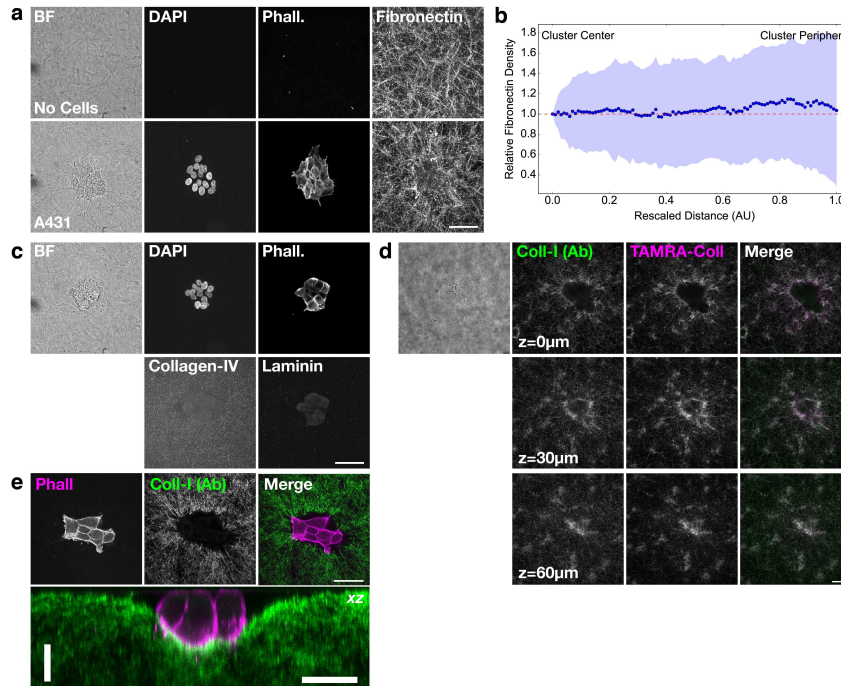
**Extended Data Fig. 6. Cell clusters do not deposit additional ECM during migration. a.** Collagen networks containing no cells or A431 clusters fixed and immunostained for Fibronectin, with additional DAPI (DNA) and Phalloidin (F-Actin) staining. The Fibronectin panel represents a brightest point projection over $25\mu$m in the $z$-axis to capture the network in the region directly under the cluster. Representative image from n=23 clusters, N=3 independent experiment. Scale bar: $50\mu$m. **b.** Average radial linescan (median$\pm$SD) of fibronectin intensity from the cluster center to the periphery from data represented in *e*. At all distances, p>0.05 for a two-tailed t-test with $\mu_0 = 1$. **c.** Collagen networks with A431 clusters seeded on top were fixed and immunostained for Collagen-IV and Laminin, with additional DAPI (DNA) and Phalloidin (F-Actin) staining. Representative image from n=5 clusters, N=1 independent experiments. Scale bar: $50\mu$m. **d.** Fluorescent TAMRA-collagen networks with A431 clusters plated on top were fixed and immunostained for

Collagen-I. Panels reflect single confocal slices at different $z$-steps. Colocalization between the TAMRA-Collagen and Collagen-I Antibody signal was R = 0.895±0.040 (mean±SD; p<0.001) from n=15 clusters, N=2 independent experiments. Scale bar: 50$\mu$m. **e.** A431 cluster plated on a collagen network, fixed and immunostained with a Collagen-I antibody plus Phalloidin and imaged by two-photon microscopy. Representative image from n=9 clusters, N=2 experiments. Horizontal scale bars: 50$\mu$m, 25$\mu$m. Vertical scale bar: 10$\mu$m.
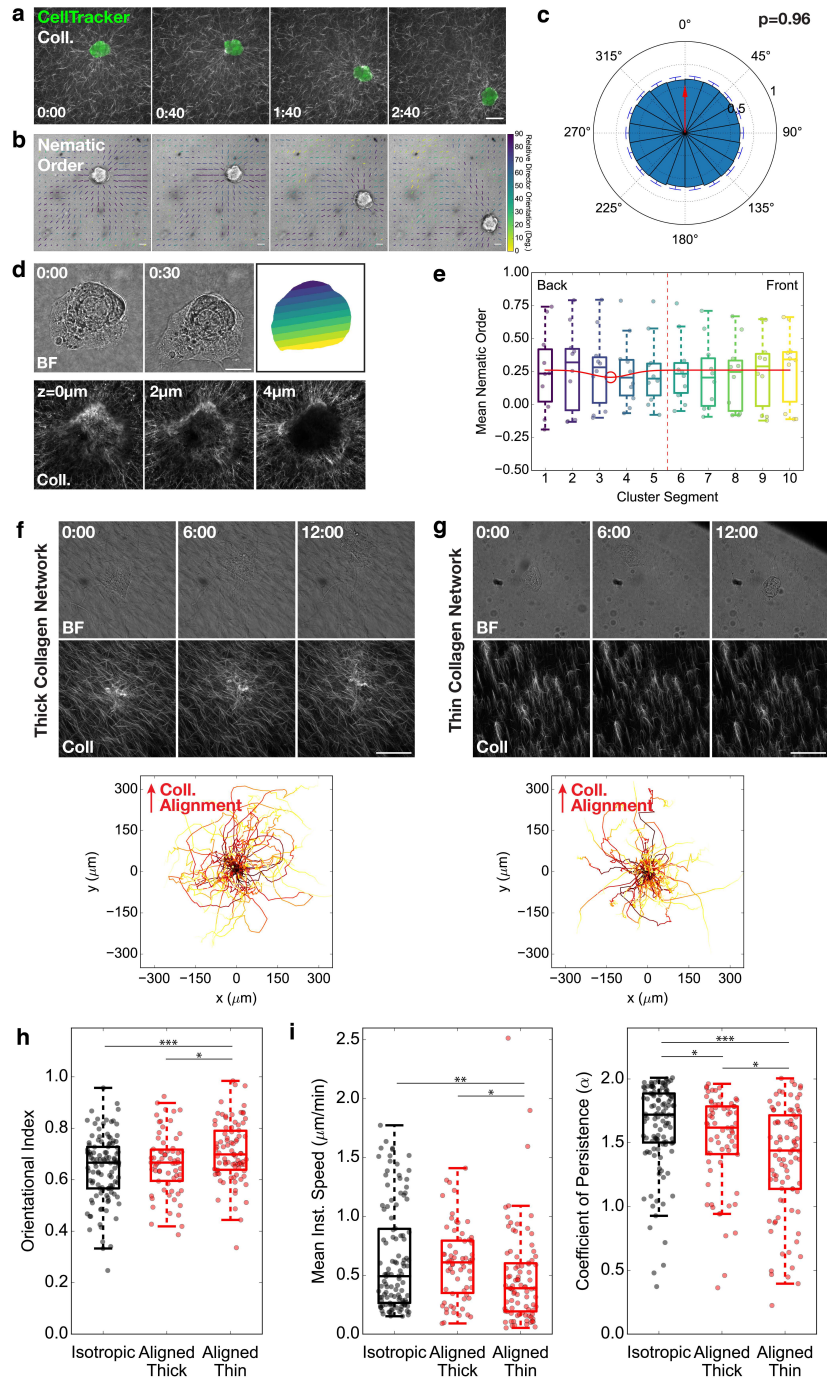
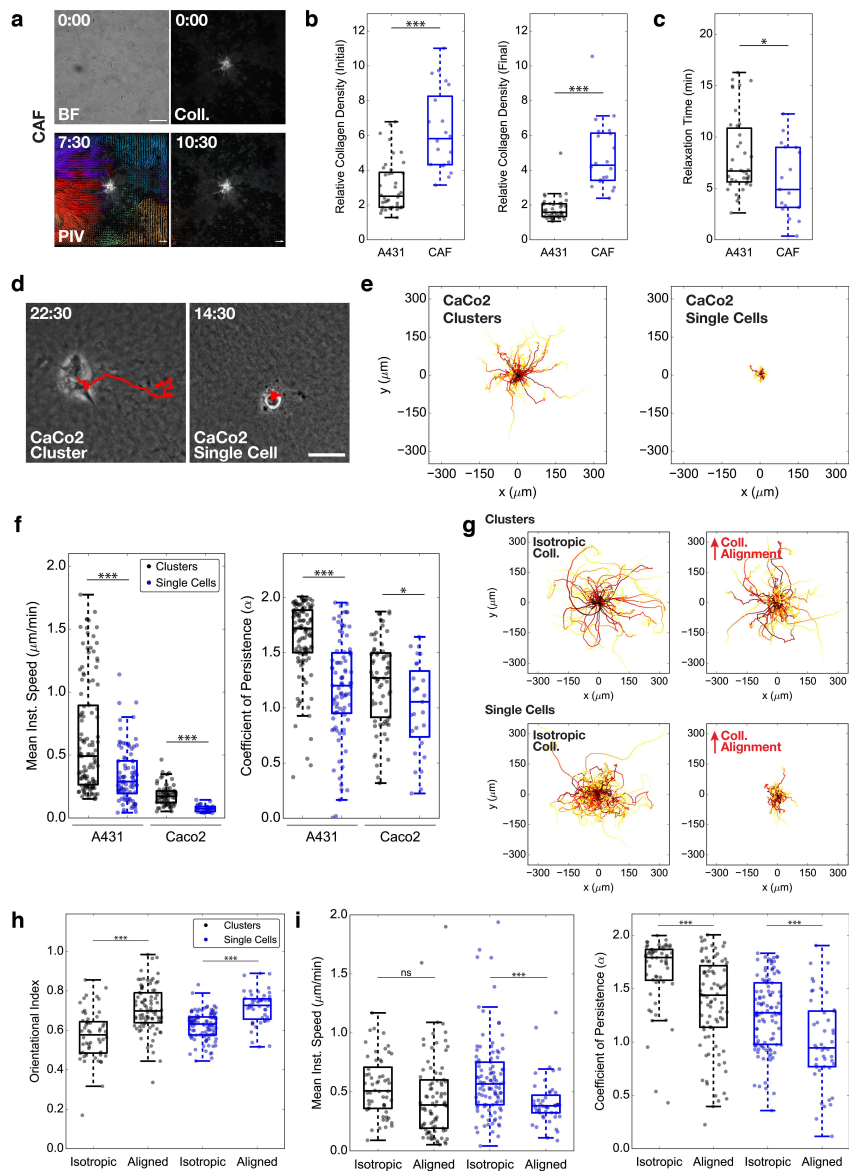**Extended Data Fig. 7. Analysis of collagen network alignment during collective migration.**

**a.** Montage of a cluster on a fluorescent collagen network (single *z*-slice on network surface). Scale

Bar: $50\mu$m. HH:MM. **b.** Montage of cluster in *a* overlaid with the local collagen alignment. Rods: local nematic order (orientation indicates mean collagen fiber orientation, length indicates order parameter magnitude $S$, color indicates orientation with respect to cluster center of mass ($90°$ is oriented toward the cluster, $0°$ is oriented perpendicular to the cluster). Scale rod: $S = 1$. Image length scale as for *a*. **c.** Polar plot of nematic order within $50\mu$m of the cluster boundary (mean$\pm$SD over all time points). P-value: Rayleigh test of uniformity. For *a-c*, representative images/data from n=28 cells, N=3 independent experiments. **d.** Live imaging of clusters using AiryScan super-resolution microscopy. *Upper Panels*: Brightfield images with segmentation and front-to-back regions in the direction of migration. *Lower Panels*: AiryScan images of TAMRA-labeled collagen at different z-positions. **e.** Box plot of the collagen fiber nematic order from AiryScan images. Dots represent individual clusters. For *d, e*, representative images/data from n=11 clusters, N=3 independent experiments. **f, g.** Montages of clusters migrating on thick deformable (*f*) or thin non-deformable (*g*) aligned collagen networks. *Lower Panels*: Overlaid cluster migration trajectories, adjusted to start at the origin (0, 0) and rotated with respect to collagen alignment direction. Scale Bars: $100\mu$m. HH:MM. Representative images from n=66, 86 clusters, N=4, 4 independent experiments **h.** Boxplot of orientational index along the collagen alignment direction for conditions in *f, g*. One-way ANOVA: p=0.00113. *p<0.05, ***p<0.001 for Tukey HSD post-hoc test (p=0.340, <0.001, 0.0184). **i.** Boxplots of mean instantaneous speed and coefficient of persistence for conditions in *f, g.*. For *h, i*, data from n=114, 66, 86 clusters, N=6, 4, 4 independent experiments. Thick isotropic data is the same as Fig. 1f. One-way ANOVAs: p=0.0180, 7.83e-6. *p<0.05, **p<0.01, ***p<0.001 for Tukey HSD post-hoc test (p=0.567, 0.00919, 0.0393; p=0.0413, <0.001, 0.0190).
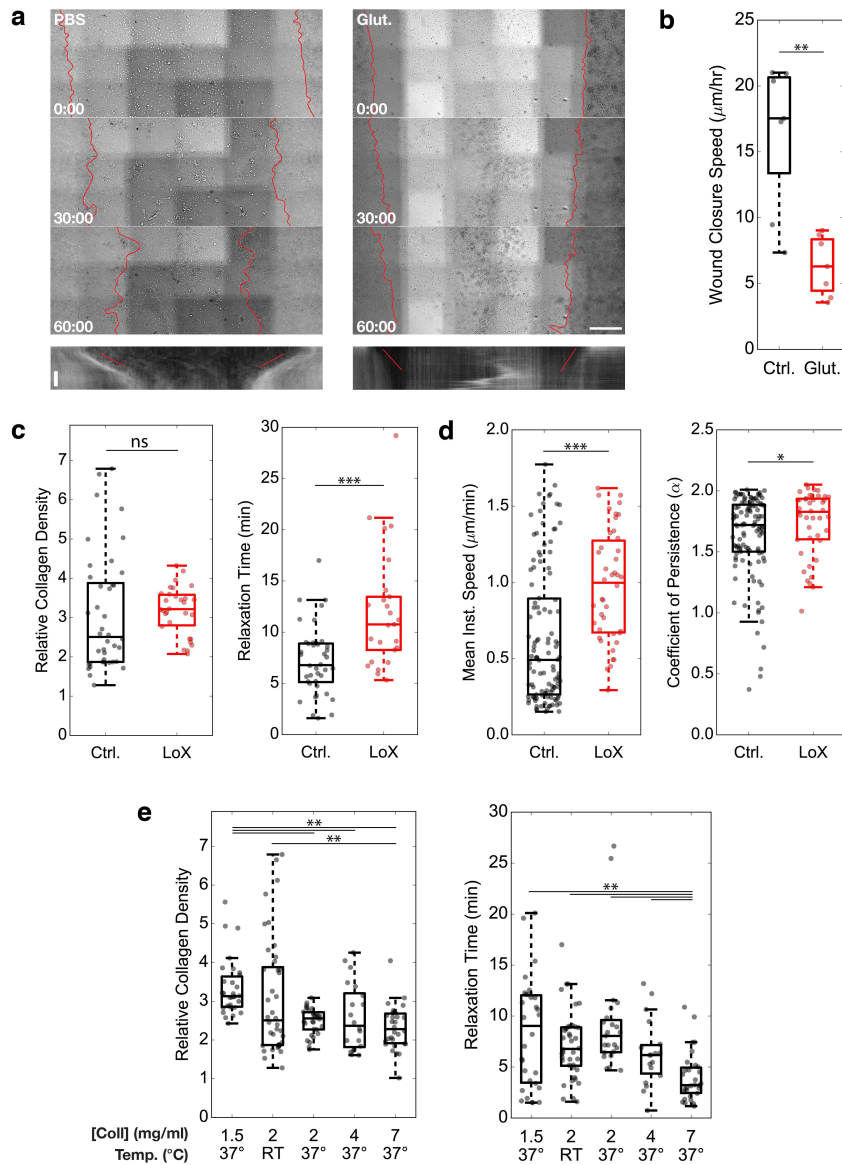
**Extended Data Fig. 8. Role of crosslinking on different migration modes. a.** Montages from wound healing assays using A431 cells plated using stencils on collagen networks pre-treated with PBS or the crosslinker glutaraldehyde. Red lines indicate the leading edge. Horizontal Scale Bar: $500\mu$m. HH:MM. *Lower Panels*: Kymograph showing progression of the leading edge over time. Red lines indicate the velocity of wound closure on each side. Vertical Scale Bar: 20 hours. **b.** Box-

plot of wound closure speed on control and crosslinked collagen gels. For *a, b*, representative images/data from n=7, 7 collagen gels, N=3, 3 independent experiments. **p<0.01 for Welch's t-test (p=0.00258). **c.** Boxplots of relative collagen density and relaxation time ($\tau_r$) following cluster removal using Trypsin/$NH_4OH$ for collagen networks treated with Lysyl Oxidase (LOX). Each dot represents one cluster that was rapidly removed. Data represents n=40, 25 clusters, N=5, 3 independent experiments. ns:p>0.05, ***p<0.001 for Welch's t-test (p=0.717, 0.000550). **d.** Boxplots of mean instantaneous speed and coefficient of persistence for cluster migration on LOX-treated collagen networks. Data represents n=114, 42 clusters, N=6, 2 independent experiments. Control data is the same data as presented in Fig. 1f. *p<0.05, ***p<0.001 for Welch's t-test (p=5.707e-6, 0.0472). **e.** Boxplots of relative collagen density (*left*) and relaxation time ($\tau_r$, *right*) following cluster removal using Trypsin/$NH_4OH$ for collagen networks using different collagen concentration or polymerization temperature. Each dot represents one cluster that was rapidly removed. Data represents n=30, 40, 23, 18, 30 clusters, N=3, 5, 3, 2, 3 independent experiments. One-way ANOVA p=8.30e-5, 5.22e-5. **p<0.01 for Tukey HSD post-hoc test (p=0.375, <0.001, 0.001665, <0.001, 0.0332, 0.176, 0.01, 0.539, 0.204, 0.195; p=0.27, 0.506, 0.159, <0.001, 0.0579, 0.373, <0.001, 0.0497, <0.001, 0.00683).

**Extended Data Fig. 9. Single cell collagen deformation and migration. a.** Micrographs of a primary human cancer associated fibroblast (CAF) on a fluorescent collagen network. Scale bar: $50\mu$m. Scale vector: $0.5\mu$m/min. HH:MM after addition of Trypsin/NH$_4$OH. Representative image from n=18 CAFs, N=2 independent experiments. **b.** Boxplots comparing relative collagen density before and after CAF removal. **c.** Boxplot of viscoelastic relaxation time ($\tau_r$) following

CAF removal. For *b, c*: each dot represents one cluster. Data from n=39, 18 clusters/CAFs, N=5, 2 independent experiments. For *b, c*, *p<0.01, ***p<0.001 for Welch's t-test (p=6.65e-6, 1.19e-6, 0.0260). **d.** Micrographs from CaCo2 single cell or cluster on collagen networks. Red: migration trajectories. Scale Bar: 50$\mu$m. HH:MM. **e.** Overlaid migration trajectories for CaCo2 single cells and clusters, adjusted to start at the origin (0, 0). **f.** Boxplots of mean instantaneous speed and coefficient of persistence for A431/CaCo2 clusters/single cells. For *c-e*, representative examples/data from n=114, 89, 69, 27 clusters/single cells, N=6, 3, 2, 2 independent experiments. A431 cluster data is same as in Fig. 1f. *p<0.05, ***p<0.001 for Welch's t-test (p=2.57e-9, 3.44e-15, 5.25e-13, 0.0185). **g.** Overlaid migration trajectories for clusters and single cells on thin isotropic or aligned collagen networks, adjusted to start at the origin (0, 0) and rotated with respect to the collagen alignment direction. **h.** Boxplot of orientational index along collagen alignment direction. **i.** Boxplots of mean instantaneous speed and coefficient of persistence. For *g-i*, Data represents n=56, 86, 103, 45 clusters, N=2, 4, 2, 2 independent experiments. Data for cluster migration on thin aligned networks is same as Extended Data Fig. 5g-i. For *h, i*, ns=p>0.05, ***p<0.001 for Welch's t-test (p=3.89e-9, 4.28e-9, 0.209, 2.30e-5, 8.74e-6, 0.000379).
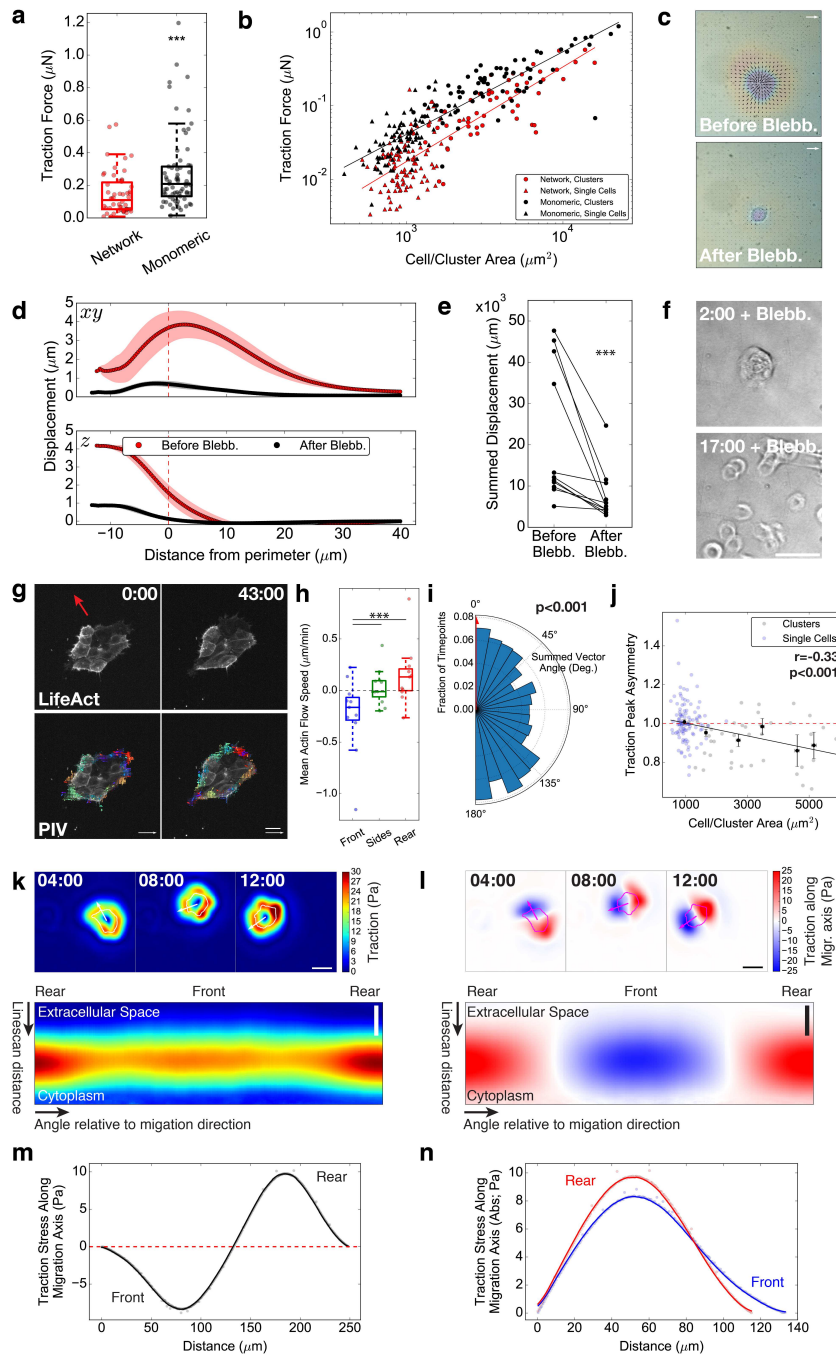
**Extended Data Fig. 10. Traction force distributions are asymmetric and require myosin-2.**

**a.** Integrated 2D tractions from clusters on PAA + thin collagen network or monomeric collagen,

n=54, 69 clusters, N=3, 3 independent experiments. ***p<0.001 for Welch's t-test. **b.** Integrated traction force vs. cluster area on PAA + collagen network or monomeric collagen. Solid lines: power-law fits. **c.** 3D displacements of a cluster on PAA gel + thin collagen network with blebbistatin. Black arrows: *xy* displacements. Color scale: *z* displacements. **d.** Mean radial traction linescans from *c*. **e.** Summed displacements before/after blebbistatin treatment, n=11 clusters, N=1 independent experiment. ***p<0.001 for Welch's t-test. **f.** Micrographs of clusters following blebbistatin treatment. Scale Bar: 100$\mu$m. HH:MM. **g.** Micrographs of mCherry-LifeAct A431 cells. Red arrow: migration direction. *Lower Panel*: PIV vectors of actin flows in the cortical region. Scale bar: 20$\mu$m. Scale vector: 0.05$\mu$m/min. MM:SS. See also Supplementary Video 22. **h.** Mean actin flow speeds with respect to migration direction for n=10 clusters, N=3 independent experiments. ***p<0.001 for Welch's t-test. **i.** Radial histogram of summed PIV vector angle with respect to the migration direction (red arrow). P-value: Rayleigh test of uniformity. **j.** Plot of traction peak asymmetry (Front/Back). Solid circles: all binned data (mean±SEM). Line: linear fit (raw data). Data represents n=54, 104 clusters/single cells, N=3, 3 independent experiments. **k, l.** Traction force magnitudes (total (*k*) or projected along migration axis (l)) for the cluster in Fig. 6a. *Lower panels*: Unfolded radial linescans with respect to the cluster front. Scale bars: 20$\mu$m. **m, n.** Linescans of tractions along migration axis (absolute values in *n*). Dots: raw values. Lines: smoothed data.